Available online at www.sciencedirect.com
SCIENCE DIRECT®
Journal of Solid State Chemistry 176 (2003) 496–529
JOURNAL OF SOLID STATE CHEMISTRY
http://elsevier.com/locate/jssc

Modeling the framework stability and catalytic activity of pure and transition metal-doped zeotypes

Furio Corà,* Maria Alfredsson, Carolyn M. Barker, Rob G. Bell, Martin D. Foster, Iman Saadoune, Alexandra Simperler, and C. Richard A. Catlow

Davy-Faraday Research Laboratory, The Royal Institution of Great Britain, 21 Albemarle Street, London W1S 4BS, UK

Received 24 January 2003; received in revised form 29 April 2003; accepted 6 May 2003

Abstract

We present a thorough computational study of transition metal-doped zeolite and aluminophosphate (AlPO) frameworks. The structural and electronic chemistry of the dopants is examined with ab initio quantum mechanical calculations, and the results correlated with the Brønsted and Lewis acid strength, and with the redox potential of the dopant ions in the framework. The energetics of doping is provided, and is employed to analyze the mode of dopant incorporation, and its site ordering in the microporous framework. In total, 23 dopant ions are examined in the isostructural framework of chabasite and AlPO-34. These cover most of the isomorphous framework replacements known to occur experimentally, but also framework replacements that have not yet been achieved. In this case, ab initio modeling techniques are employed in a predictive way. Finally, we present a computational study of the alkene epoxidation on titanosilicates, that covers the whole catalytic cycle.

Keywords: Zeolites; AlPOs; Transition metaldopant; Heterogenous catalysis; Catalytic activity; Acidity; Reaction modeling

1. Introduction

Under the common name of zeotypes, we identify a family of crystalline oxides built up from corner-shared TO_4 tetrahedra (T=Si, Al, Ga, P), whose structure contains internal cavities and channels of size comparable to that of small organic molecules [1]. The microporous architecture allows molecules to selectively diffuse through and react within the solid, and enables an accurate control and design, at the atomic level, of the processes that can occur within the solid [2]. The similarity of these properties with the high molecular recognition capability and catalytic activity of enzymes [3] motivates the flourish of research activity on zeotypes, with the dual goal of (a) synthesizing new microporous architectures with enhanced size-shape selectivity and (b) including a range of catalytically active sites within the solid.

The first goal is pursued both with the synthesis of novel microporous polymorphic structures, aided by the use of structure-directing (template) molecules during the synthesis [1,4,5], but also by varying their chemical composition. Indeed, the exceptional structural and chemical diversity of microporous solids arises in part from the growing range of chemical building blocks from which these materials are constructed. The original family of aluminosilicates and silica-based zeolites has been greatly extended in recent decades, to include aluminophosphates (AlPOs) and gallophosphates (GaPOs) [6,7], as well as hybrid organic/inorganic frameworks and microporous transition metal oxides [8]. In this paper we focus on the solid-state chemistry of zeolites and AlPOs, whose framework has composition SiO_2 and $AlPO_4$, which are the microporous materials that display the richest polymorphic behavior, and hence are the most widely studied. The aluminophosphate framework can be imagined as obtained from the isostructural zeolite by replacing pairs of Si^{4+} ions with strictly alternating Al^{3+} and P^{5+} ions in the tetrahedral sites.

The catalytic activity of zeotypes is associated with the presence of framework defects. In the stoichiometric SiO_2 or $AlPO_4$ form, the zeotypic framework is chemically inert. If, however, a charge imbalance occurs in the framework, for instance by replacing a Si^{4+} ion

*Corresponding author. Fax: +44-2076-293569.
E-mail address: furio@ri.ac.uk (F. Corà).

0022-4596/03/$ - see front matter © 2003 Elsevier Inc. All rights reserved.
doi:10.1016/S0022-4596(03)00275-5

with Al^{3+} in zeolites, or P^{5+} by Si^{4+} in AlPOs, the framework is chemically activated. The overall negative charge of the tetrahedral backbone is compensated during the synthesis by extraframework cations, often the same molecules acting as templates to direct the synthesis towards the microporous structure. In this case, the extraframework cations are replaced by protons during calcination, yielding Brønsted acid sites in the solid [9,10].

The catalytic activity can be further modified by the introduction in the framework of new heteroatoms, including transition metal ions such as Ti, Fe, Co and Mn, which open up new catalytic opportunities in the field of selective and partial oxidation catalysis [2,11,12]. Despite their structural similarity to zeolites, AlPOs are able to accommodate more types of framework heteroatoms and at higher concentrations [13]; the catalytic behavior resulting from the inclusion of these dopant ions, however, is still poorly understood. Further characterization work of the doped frameworks is needed, in order to understand the structural and electronic properties associated with different dopant ions in zeolites and AlPOs, and how the chemistry of the dopants is influenced by their constrained environment in the microporous framework. This knowledge is crucial to gain control of the activity associated with different types and concentrations of heteroatoms. Rationalizing the chemistry of the transition metal dopants in the zeolite and AlPO frameworks is therefore a subject of considerable practical interest.

The unique structural features of microporous oxides make these materials of interest also in fundamental research. In dense heterogeneous catalysts, the active sites are located on the external surfaces of the solid, where they are of difficult characterization (especially in situ and during operating conditions) because of their low concentration and of the low surface-specificity of most experimental techniques. In microporous oxides, instead, reactants are in contact with the internal surfaces of the solid, and the active sites are uniformly distributed in the bulk, not only on the external surfaces, where they can be accurately characterized by a wider range of solid-state techniques [14].

If the inclusion of the dopant in the framework is long-range ordered, its local environment can be investigated by powerful diffraction methods. This is rarely the case, except at very high concentrations (see, e.g., [15,16]); low levels of doping usually result in a disordered incorporation of the dopants in the zeotypic framework. In this case, structural information on the dopants can be derived by means of element-specific spectroscopic techniques, such as X-ray absorption spectroscopy (XAS), and in particular EXAFS [17]. However, EXAFS studies provide average values for the selected element over the whole material; when more than one coordination environment and/or oxidation state are present, the experimental result is a weighted average of all the local environmental structures in which the dopant ions are hosted (see, e.g., [18–20]). For a proper characterization of the catalyst, it would be desirable to have means to investigate each local environment independently.

Computer modeling techniques allow an easy control of the structural and electronic parameters of the system, such as the oxidation state of the active site and the composition of the material. Modeling is therefore an increasingly important characterization tool to investigate the structural chemistry of complex materials [21]. In zeolite science, modeling can provide accurate information on the structure and chemistry of the active sites, and in this paper we apply a combination of modeling methodologies to study crucial features of the zeolite and AlPO chemistry, related both to the framework stability, and to the activation of the framework with transition metal dopant ions.

2. Computational methods

A wide range of computational techniques available to solid-state scientists can contribute to understand different aspects of the chemistry of pure and doped zeotypic frameworks. Methods based on interatomic potentials (IP) provide valuable information about the structural stability of different framework architectures, and on the structural strain caused by the inclusion of dopant ions with different size and/or charge. The study of electronic properties, such as the relative stability of different electronic and spin states of transition metal dopants, is accessible by the use of Quantum Mechanical (QM) methods, where the treatment of the electronic, not only structural, degrees of freedom is taken explicitly into account.

Not only the Hamiltonian, but also the model of the solid offers different choices when applied to the study of zeotypes. The extended nature of crystalline materials is best suited for techniques that employ periodic boundary conditions; however, the local nature of the chemistry in the framework of zeolites and AlPOs is such that small molecular fragments cut out of the three-dimensional solid are representative enough to include the major contributions to the chemical reactivity of the active sites. Molecular calculations, in which the crystalline environment of the active site is treated with a low level of accuracy, are therefore also able to provide valuable insight into the chemistry and reactivity of zeotypes [22–24].

The wide range of problems associated with the presence of transition metal ions in zeolites and AlPOs, requires us to use a combination of different computational techniques. The calculations described in the following sections have therefore been performed with

different methods and codes, of which here we briefly summarize the details.

2.1. Interatomic potential techniques

Accurate IP to describe the undoped framework of zeolites and AlPOs are available in the literature [25,26]; they make use of formal ionic charges, of Buckingham potentials to represent two body repulsion forces, and include a core-shell description of the oxygen polarizability. Structural constraints are included via three-body terms centred on the tetrahedral ions. In our IP calculations we employed the GULP program [27], using periodic boundary conditions, and the parameterization of Refs. [25] for zeolites and [26] for AlPOs.

To examine systematically with IP calculations the replacement of a framework T site with dopant ions of different size, we can modify the pre-exponential parameter A of the T–O Buckingham potential, in which the interaction energy between a pair of ions i and j in the structure is given by

$$E_{ij} = A_{ij} \exp\left[-r_{ij}/\rho_{ij}\right] + \{-C_{ij}/r_{ij}^6 + Q_i Q_j / r_{ij}\}. \quad (1)$$

The $i-j$ bond distance is related to the value of the parameters A and ρ. Assuming a Huggins–Mayer relationship, if r_o is the equilibrium interatomic separation, then

$$A = \exp\left[r_o/\rho\right]. \quad (2)$$

When r_o varies by an amount Δr due to a change in size of the metal dopant, the pre-exponential factor A is modified as follows:

$$A' = A \exp\left[\Delta r/\rho\right]. \quad (3)$$

Vice versa, a change in A modifies the ionic radius of the ion according to

$$\Delta r = \rho \ln A'/A. \quad (4)$$

By varying the pre-exponential factor of the Buckingham potential, we can therefore modify, in a continuous way, the size of the dopant ion included in the framework.

2.2. Periodic QM calculations

Periodic QM calculations have been performed employing the computer code CRYSTAL [28,29]. We employed a local basis set of at least split-valence plus polarization functions for each atom of the structure; the basis functions are available from the online library of the code [30], and are described in Ref. [31]. Each structure examined in the following sections has been optimized (using space group $P1$ to not impose symmetry constraints on the solution), employing the analytical evaluation of forces [32,33], which is included in a pre-released version made available to us by the authors.

In our calculations we first compared the performance of different Hamiltonians, ranging from the Hartree-Fock (HF) to local [34] or gradient-corrected [35] density functionals (DF), to the HF-DF hybrid scheme (B3LYP) proposed by Becke [36] to describe the equilibrium structure of berlinite and of the simplest microporous AlPO polymorphs. Since all the Hamiltonians provide results in good overall agreement, subsequent calculations on the doped materials have been performed only at the (unrestricted) HF level. Several transition metal dopants successfully introduced in zeolite and AlPO frameworks are open-shell ions with unpaired electrons, for which an UHF study represents a valuable choice. This Hamiltonian employs the exact expression of exchange forces, which are known to be important for a correct representation of the unpaired electrons [37].

2.3. Molecular QM calculations

Molecular QM calculations have been performed to study the reaction mechanism leading to the epoxidation of alkenes on titanosilicates. A molecular cluster model of the Ti-centred active site has been employed, consisting of a $(H_3SiO–)_3Ti–OH$ fragment which extends two coordination spheres from the Ti dopant. In selected cases, a larger cluster including the third coordination sphere of Ti has also been used. The clusters were cut from a siliceous silicalite (MFI) framework, with all severed bonds saturated by hydrogens. The fragment geometry (with Ti replacing the central Si) has been first optimized keeping the outermost framework atoms fixed. After this optimization step, in the study of transformations taking place during the catalytic cycle, also the outermost Si atoms have been fixed, to represent the rigidity of the silica framework. This procedure may over constrain the cluster [38], but is most certainly a better approximation than allowing complete relaxation of an unconstrained fragment.

DFT-GGA cluster calculations, employing the Becke exchange [39] and the Perdew–Wang correlation [40] functionals, have been performed with the codes DGAUSS [41] and DMOL [42]. The former enables the analytical evaluation of the second derivatives of the energy with respect to the nuclear coordinates, which is particularly valuable in the search of transition states during the study of reactivity. DMOL, instead, has been employed for all the geometry optimizations. In both cases, we used a double ξ plus polarization basis set, as detailed in Ref. [43].

3. Results and discussion: chemistry of the undoped zeolite and ALPO frameworks

A proper characterization of the tetrahedral backbone in zeolites and AlPOs is a valuable starting point in

order to understand the chemistry that follows the framework incorporation of transition metal ions. We shall therefore start our discussion in this section with the results of calculations, both QM and IP, performed on the undoped materials; studies of the doped frameworks will follow in Sections 4–6.

3.1. Nature of the bonding

We studied with periodic QM calculations four different zeolitic frameworks with a small unit cell (a maximum of 36 atoms), namely α-quartz, sodalite, chabazite and ATN, and their isostructural AlPOs: berlinite, AlPO-20, AlPO-34 and AlPO-39.

In Table 1 we report the geometry-optimized structure of berlinite, the AlPO polymorph for which the most accurate experimental structural studies are available [44,45]. A consistent study on zeolites is available in literature [46]. The excellent agreement between calculated and experimental values gives confidence in the quality of our calculations. Only the DF calculations in the local density approximation yield a noticeable structural difference, with the usual underestimation ($\approx$1–2%) of the lattice parameters, due to an overestimation of the non-bonded (van der Waals) interactions. The latter modify appreciably the Al–O–P angles in the structure, and suggest that LDA calculations are not adequate for the study of zeotypes.

The framework properties of microporous AlPOs are often assumed to match closely those of the isostructural SiO_2 polymorph; the long-range ordered alternance of Al^{3+} and P^{5+} cations is in fact assumed to balance their chemical difference. The results of our calculations show instead that the bonding features of the framework Al, Si and P atoms with the oxygens are different. In Table 2 we report the calculated atomic charges in quartz and berlinite, defined via a Mulliken partition scheme; for each Hamiltonian employed, the other polymorphs examined show only minor differences, of less than 0.01 $|e|$, suggesting that the bonding features are a local property of the solid, not affected by the crystalline environment. Net charges and bond populations indicate that the Si–O bond in zeolites and the P–O bond in AlPOs are covalent, while the Al–O interaction in AlPOs is ionic. The net charges of Si and P are less than half their formal value of +4 and +5, and the Si–O and P–O bonds have an overlap population (of 0.31 and 0.27 electrons with the B3LYP Hamiltonian) that is almost twice the value of the Al–O bonds (0.17 electrons). To support this finding, in the left column of Fig. 1 we show two difference electron density maps, obtained by subtracting the density of isolated formal ions from

Table 1
Comparison of the calculated and experimental crystal structure of berlinite

	Expt. [44]	Expt. [45]	B3LYP	HF	LDA	GGA
a (Å)	4.9429	4.9423	4.9442	4.9430	4.8161	4.9444
c (Å)	10.9476	10.9446	10.9463	10.9452	10.9115	10.9470
x (Al)	0.4660	0.4664	0.4644	0.4659	0.4584	0.4631
x (P)	0.4675	0.4669	0.4636	0.4652	0.4537	0.4627
x (O1)	0.4220	0.4163	0.4135	0.4186	0.4114	0.4114
y (O1)	0.2960	0.2922	0.2965	0.2953	0.3107	0.2994
z (O1)	0.3964	0.3977	0.3950	0.3976	0.3917	0.3933
x (O2)	0.4090	0.4156	0.4130	0.4166	0.4039	0.4106
y (O2)	0.2520	0.2576	0.2637	0.2592	0.2754	0.2663
z (O2)	0.8868	0.8837	0.8811	0.8830	0.8769	0.8795
r(Al–O)	1.729	1.736	1.745	1.740	1.738	1.753
r(P–O)	1.525	1.521	1.539	1.518	1.537	1.549

Space group $P3_121$; the *y* and *z* fractional coordinates of the Al and P atoms are (0,1/3) and (0,5/6), respectively. The bottom rows refer to the average *T*–O bond distance, *r*, in Å.

Table 2
Calculated net atomic charges (Q) and *T*–O bond populations (Q_b), in $|e|$, defined via a Mulliken partition scheme for berlinite and quartz, studied with different ab initio QM Hamiltonians

Berlinite	B3LYP	HF	LDA	GGA	Quartz	B3LYP
Q (Al)	+1.95	+2.19	+1.80	+1.90	Q(Si)	+1.50
Q (P)	+2.25	+2.85	+1.94	+2.11		
Q (O1)	−1.04	−1.26	−0.93	−1.00	Q(O1)	−0.75
Q (O2)	−1.05	−1.26	−0.94	−1.01	Q(O2)	−0.75
Q_b(Al–O)	0.17	0.14	0.18	0.17		
Q_b(P–O)	0.27	0.27	0.26	0.26	Q_b(Si–O)	0.31

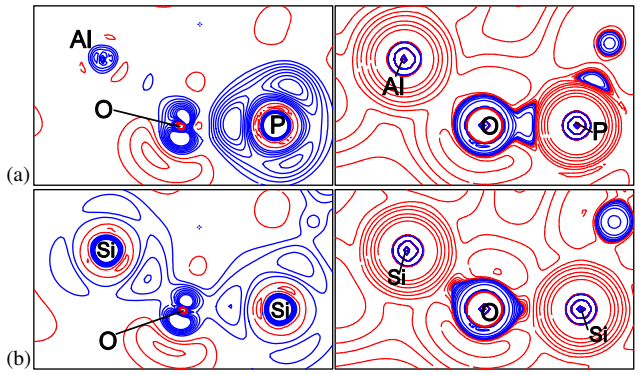

Fig. 1. Difference electron density map (solid minus isolated formal ions) (left plots), and Laplacian, L, of the electron density (right plots), in a plane containing one Al–O–P (a) or Si–O–Si (b) unit in berlinite and quartz. Continuous and dotted lines in the left plots correspond to positive and negative densities; in the right plots, continuous lines define the regions of negative L and covalent T–O interaction, dashed lines correspond to zones of positive L and ionic interaction. The calculations have been performed with the B3LYP Hamiltonian.

the total electron density of the solid. The maps are drawn in a plane containing one Al–O–P, or the corresponding Si–O–Si unit, in quartz and berlinite. Via these maps, we can compare the population of the valence atomic orbitals on the tetrahedral (T) species (T = Al, Si and P) with a perfectly ionic solution; the more electrons are associated with the T ion, the more its bonding with the oxygens is covalent. While the difference density shows no feature on Al, which can be described as ionic, an important fraction of the valence electron density is associated with Si, and even more so with P. The electronic redistribution shows clear maxima in the Si–O and P–O directions, indicative of their covalent bonding.

An alternative description of the bonding can be achieved by means of the Quantum Theory of Atoms in Molecules, proposed by Bader [47]. In regions of ionic interaction, the (calculated) electron density ρ shows minima along the bonds, and has a positive curvature; the regions of covalent bonding, instead, correspond to local maxima of ρ, where the curvature is negative. By calculating and mapping the Laplacian of the calculated electronic density ($L = \nabla^2\rho$), we can therefore detect the regions of ionic and covalent interaction in the solid. In the right column of Fig. 1 we report the Laplacian of the calculated electronic density, from our B3LYP study. In AlPOs there is an ample zone of negative L along the P–O bond, which is described as covalent. The Al–O bond, instead, has positive L, with only a minor distortion of the electronic shell on the oxygen towards Al. The Si–O bond in zeolites has intermediate behavior between the Al–O and P–O bonds, but still causes a distortion of the electron density around the oxygen. A small area of negative L is present along the Si–O directions.

All the above arguments give unambiguous information on the nature of the bonding: AlPO frameworks comprise discrete Al^{3+} and PO_4^{3-} ionic units, rather than the continuous semicovalent network present in zeolites. This result confirms the indication arising from earlier experimental studies [44], and agrees with the more hydrophilic nature of AlPOs compared to zeolites, also known from experiment. AlPO-34, for instance, is reversibly hydrated [48], while the isostructural chabasite (as all defect-free zeolites) is hydrophobic. The molecular-ionic nature of AlPOs has important consequences for our understanding of the defect chemistry, as we shall see in Section 4; ionic substitutional dopants are expected to replace more readily Al in AlPOs than Si in zeolites.

3.2. Structural stability of the undoped frameworks

In order to identify which factors are important to define the structural stability of zeolites and AlPOs, and enable their rich polymorphic behavior, we have performed a systematic investigation with IP techniques of a set of their known polymorphic structures (listed in Table 3). Given the relatively high number of polymorphs available, these data can be employed to perform a useful statistical analysis of their structural features. In the following of the discussion we shall investigate the dependence of the calculated lattice energy on framework density, coordination sequences, average bond distances and angles, and distortion of the TO_4 tetrahedra in the structure. All data refer to structures in their calculated equilibrium geometry. It is important to notice that many known AlPO polymorphs share the same structure of known zeolites; others, however, have unique framework types, and they can have very large ring structures, such as the 18-ring channel in VPI-5, that are not common in zeolites. We expect therefore a similar, but not identical dependence of the calculated energy on the structural parameters listed above for AlPOs and zeolites.

A comparison of the experimental enthalpies ($\Delta H_{trans,298\,K}$) [49–53] and calculated relative lattice energies (ΔE_{latt}) for a selection of zeolites and AlPOs relative to quartz and berlinite, reported in Table 4, shows that the calculations reproduce well the experimental trend. We find that AlPOs are more stable relative to berlinite than zeolites are relative to quartz, in agreement with experiment, although QM calculations on a subset of structures reverse this result [54].

To rationalize the factors that control the polymorphic stability of zeolites and AlPOs, in Figs. 2–4 we plot the dependence of their calculated internal energy on several structural parameters. Fig. 2a shows the lattice energies as a function of the framework density, calculated as the number of T-sites per 1000 Å^3 in the materials. The good correlation of these two observables for both zeolites and AlPOs shows that the framework density is an important parameter to characterize the

Table 3
List of the microporous framework types investigated

Zeolites	AFG(3), ASV(2), BEA(9), BIK(2), BOG(6), BRE(4), CAS(3), CFI(5), CON(7), DAC(4), DDR(7), DOH(4), DON(5), EAB(2), EMT(4), EPI(3), ESV(6), EUO(10), FER(4), FRA(6), GME(1), GON(4), GOO(5), HEU(5), IFR(4), ISV(5), ITE(4), JBW(2), KFI(1), LIO(4), LOV(3), LTN(4), MAZ(2), MEI(4), MEL(7), MEP(3), MFI(12), MFS(8), MON(1), MOR(4), MSO(3), MTF(6), MTN(3), MTT(7), MTW(7), MWW(8), NAT(2), NES(7), NON(5), OFF(2), OSO(2), PAU(8), RSN(5), RTE(3), RTH(4), RUT(5), SFE(7), SFF(8), SGT(4),STF(5), STI(4), STT(16), TER(8), TON(4), TSC(2), VET(5), VNI(7), VSV(3), YUG(2)
Both zeolites and AlPOs	ABW(1), AET(5), AFI(1), AFX(2), ANA(1), AST(2), BPH(3), CAN(1), CGS(4), CHA(1), DFT(1), EDI(2), ERI(2), FAU(1), GIS(1), LAU(3), LEV(2), LOS(2), LTA(1), LTL(2), MER(1), PHI(2), RHO(1), SOD(1), THO(3)
AlPOs	ACO(1), AEI(3), AEL(3), AEN(3), AFN(4), AFO(4), AFR(4), AFS(3), AFT(3), AFY(2), AHT(2), APC(2), APD(2), ATN(1), ATO(1), ATS(3), ATT(2), ATV(2), AWO(3), AWW(2), CGF(5), CZP(3), DFO(6), OSI(3), SAO(4), SAS(2), SAT(2), SAV(3), SBE(4), SBS(4), SBT(4), VFI(2), WEI(2), ZON(4)

Top row: materials studied only as zeolites; bottom row: frameworks studied only as AlPOs; middle row: frameworks studied as both zeolite and AlPO. The numbers in parenthesis indicate the number of crystallographically different T-sites in each framework type.

Table 4
Experimental enthalpies of transition, $\Delta H_{trans,298\,K}$, and calculated lattice energies, ΔE_{latt}, of AlPOs and zeolites, relative to berlinite and quartz, in kJ per mole of TO_2 units

	$\Delta H_{trans,298\,K}$ AlPO	$\Delta H_{trans,298\,K}$ ZEO	ΔE_{latt} AlPO	ΔE_{latt} ZEO
α-cristobalite	3.05[a]	2.48[b]	−1.5	3.2
AEL	6.19[a]		4.0	11.0
AET	5.77[a]		7.3	14.4
AFI	7.01[a]	7.20[c]	5.3	11.7
AST		10.86[d]	11.4	18.1
BEA		9.29[d]		14.4
CFI		8.82[d]		13.0
CHA		11.43[d]	8.6	16.3
FAU		13.60[c]	13.2	19.9
FER		6.60[c]		11.8
IFR		10.04[d]		15.0
ISV		14.37[d]		16.4
ITE		10.08[d]		14.1
LTA	7.78[a]		11.7	19.3
MEI		13.90[e]		
MEL		8.19[d]		10.8
MFI		6.78[d]		10.0
MTW		8.70[c]		8.1
MWW		10.42[d]		14.7
STT		9.19[d]		14.7
VFI	8.37[a]		10.9	21.1

Experimental data are from.
[a] Ref. [49].
[b] Ref. [50].
[c] Ref. [51].
[d] Ref. [52].
[e] Ref. [53].

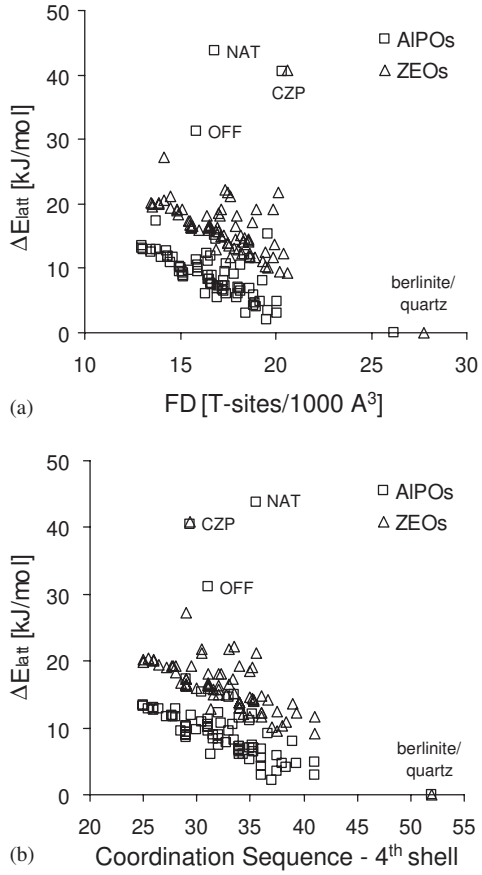

Fig. 2. Dependence of the calculated lattice energy in zeolite and AlPO structures on (a) the framework density (FD) and (b) the coordination sequence of T sites in the framework.

polymorphs. In particular, frameworks of high density are more stable than those with big voids and channel structures, due to the higher Madelung field that increases the Coulombic contribution to the bonding. The same effect was found to hold also in different polymorphic structures of transition metal oxides, such as MoO_3 and WO_3 [55]. In the set of zeotypes investigated, the framework density ranges between 13 and 20 T-sites per 1000 Å^3 for the microporous frameworks, while it is 26.2 for berlinite and 27.7 for quartz. The OFF, NAT and CZP frameworks, which do not obey the stability-density relationship observed for the other polymorphs, are also known experimentally to be less stable: OFF and NAT are known only as zeolites

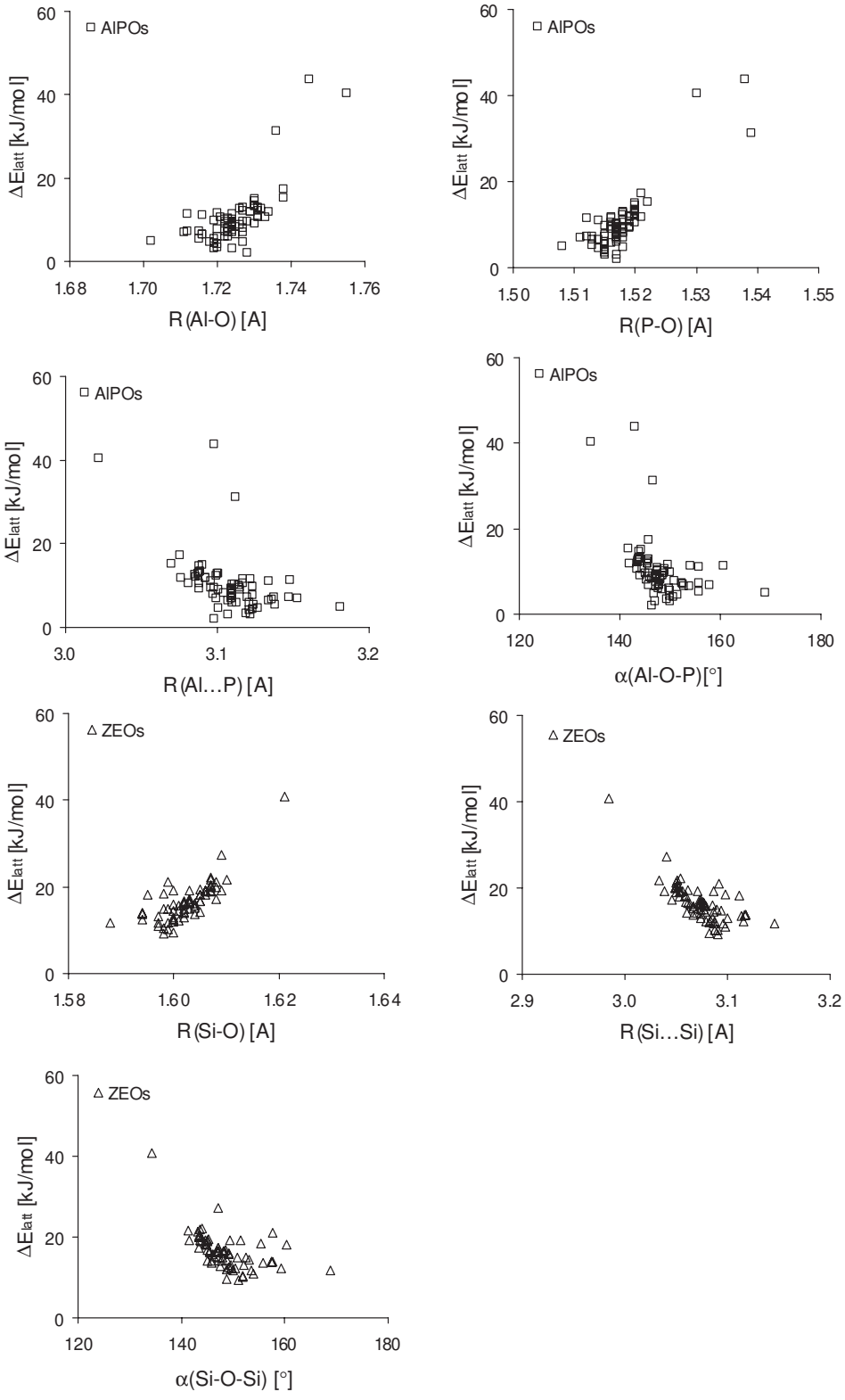

Fig. 3. Dependence of the calculated lattice energy in zeolite and AlPO structures on the equilibrium bond distances (R) and T–O–T angles (α) as indicated.

but not as AlPOs [56], while the CZP structure is known experimentally only for a zinc phosphate material [56]. Fig. 2b shows plots of the relative lattice energies as a function of the coordination sequence of the 4th shell, i.e. the number of unique 4th neighbor T sites of a given cation in the structure. The coordination sequence

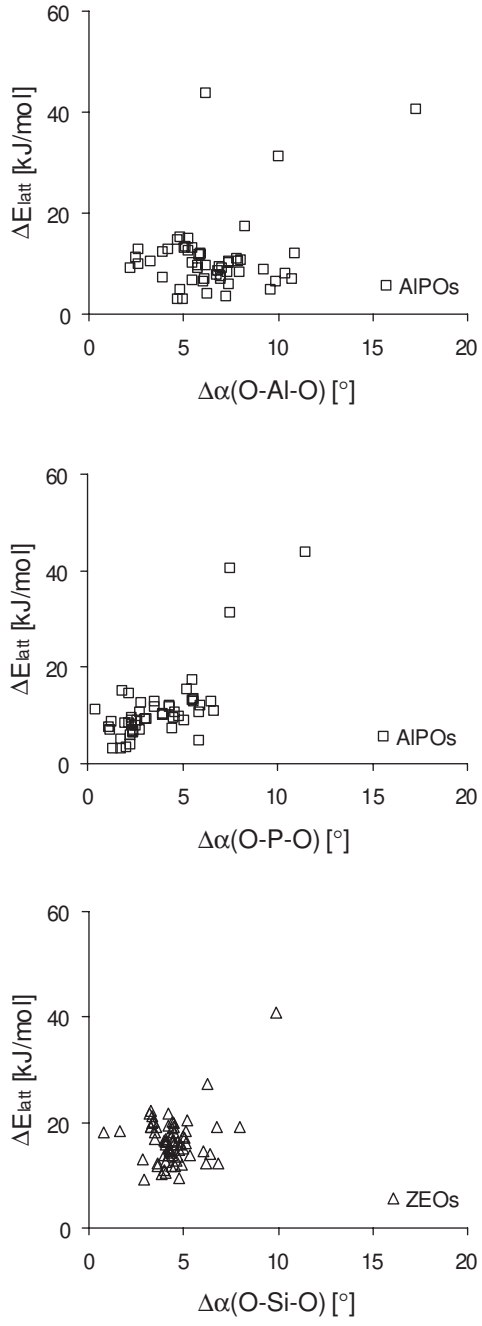

Fig. 4. Dependence of the calculated lattice energy in zeolite and AlPO structures on the structural distortion $\Delta\alpha$ (OTO) in the framework T sites.

plotted in the figure is the average value among all the crystallographic different T-sites in the structure. These plots resemble those of Fig. 2a, as the coordination sequence can be seen as a measure of the framework density: each T atom is connected to four neighbors, which themselves have four neighbors, and so on. The maximum number of T sites in the kth shell [56] is $N_k = 4 \times 3^{k-1}$; the 4th shell can have no more than 108 T-atoms. Lower numbers indicate the presence of cross linkages (rings) within the framework, which are usually channel walls or openings into voids. Hence, a low number in the coordination sequence is associated with the presence of channels and voids in the structure, which make it thermodynamically less stable, as seen in Fig. 2b. Among the microporous frameworks we find coordination sequence values between 25 and 41, while the coordination sequence for berlinite/quartz is 52. Both are substantially lower than the maximum value of 108, suggesting that a minimum number of cross linkages between T sites is required to stabilize the structure, but that too many cross-linkages introduce a structural strain, probably due to the formation of small ring structures, that destabilizes the polymorph. This structural constraint poses an upper limit to the framework density achievable in stable zeotypic networks.

In Fig. 3 we plot the calculated energy as a function of the average bond distances, $R(T-\mathrm{O})$ and $R(T\ldots T)$, and $\alpha(T\text{–O–}T)$ angles. AlPOs have Al–O bond lengths between 1.70 and 1.76 Å and P–O bond lengths between 1.51 and 1.54 Å; R(Si–O) in zeolites varies between 1.58 and 1.62 Å. The range covered is relatively small, considering the wide range of polymorphs investigated: 0.05 Å for R(Al–O), 0.04 Å for R(Si–O) and 0.03 Å for R(P–O), respectively. The distances between adjacent T-sites in AlPOs, R(Al…P), are between 3.0 and 3.2 Å; this range is achieved by a variation of the Al–O–P angle, that covers values from 134° to 169°. The distance between two neighbor T sites in zeolites, R(Si…Si), is distributed around 3.08 Å; the Si–O–Si angle varies between 140° and 160°, comparable to the value in AlPOs. We have further calculated the difference between the most obtuse and the most acute tetrahedral angles, Δ(O–T–O), which indicates the distortion and structural strain within a TO_4 unit of the solid. Results are plotted in Fig. 4. We find that differences between the tetrahedral angles in a TO_4 unit increase in the order of Al < Si < P. No clear trend is noticeable in the relative energy as a function of Δ(O–Al–O), while we find a more pronounced correlation as a function of Δ(O–P–O). Si has an intermediate behavior. This result is consistent with the type of bonding found in our QM calculations: the ionic Al^{3+} species introduces little angular strain in the AlO_4 tetrahedra, compared with the covalent PO_4^{3-} unit, where angular constraints are much more important.

There is no clear dependence between stability and short-range structural parameters; the local structural constraints do not therefore define the framework stability. We interpret this result as indicative that the local geometry of the T sites can easily adapt to the three-dimensional connectivity of the structure; the T–O bonds can be partially stretched, and the T–O–T angles easily bent without a high energetic toll. This feature is crucial to enable the wide polymorphic variety observed in zeolites and AlPOs. The features related to the framework connectivity, i.e. the degree of cross linkages

and the size of rings within the structure, are more important factors to explain the stability of the polymorphic structures.

With the increasing power of current computational techniques, mathematical expressions have been defined to enumerate and generate all the possible zeolitic frameworks compatible with the tetrahedral TO_4 building blocks [57–59]. With a proper understanding of the framework chemistry and stability, IP techniques such as those employed here can be used to evaluate the stability of these structures and the feasibility of their synthesis [60,61], thus opening up new opportunities in the search of new microporous materials with improved molecular recognition properties for application in heterogeneous catalysis.

4. Framework replacements

After studying the undoped tetrahedral backbone of zeolites and AlPOs, we shall examine the chemistry that follows the introduction in the framework of different dopant ions. Several points are of interest; we start in Section 4.1 with a study of the structural details of isomorphous replacements in the framework, followed by a characterization of the chemical features of different dopant ions, and by the calculated energetics of the doping. Other structural features, such as the long-range ordering of framework dopants and the effect of extraframework ions are described in Sections 4.4 and 4.5.

4.1. Structural parameters of dopant ions in zeolites and AlPOs

We have investigated, using periodic ab initio QM calculations, the inclusion of several 3+ dopant ions in chabasite, and of 2+ and 3+ dopant ions in its isostructural AlPO-34. The choice of this framework architecture is due to the relevance of doped chabasite and AlPO-34 to heterogeneous catalysis, coupled with the limited unit cell size (composed of 36 atoms in the undoped materials), which makes this study feasible on a routine scale with accurate QM calculations. Low valence dopant ions have been charge-compensated by protonating one of the framework oxygens that are nearest neighbor to the dopant. In the description of the doped systems we use the following symbols: M is the dopant ion; O_n $(n = 1-4)$ its nearest neighbor oxygens, in order of increasing distance from M. For low valence dopant ions charge-compensated by a Brønsted acid proton, O_H is the protonated framework oxygen. T is a generic T site of the framework, which can include also the site hosting the dopant ion. Here and in the following sections, the doped chabasite and AlPO-34 frameworks are described with periodic boundary conditions, with one dopant ion in each unit cell of the host. Even at this high concentration, compared to the level of doping achievable experimentally, the dopant ions are separated by more than 10 Å from each other, and represent therefore non-interacting defect centers. The structure of each doped framework has been optimized.

The structural parameters that describe the local environment of the M dopants in chabasite and AlPO-34, as obtained from our QM structural optimization, and from experimental data where available, are summarized in Table 5. These include the four M–O bond distances, $R(M\text{–}O_n)$, between the dopant and its four nearest neighbor oxygens; the average M–O bond distance, $\langle R \rangle$; and the M–O–T angles around the oxygens nearest neighbors of M. We also report the value of the T–O–T angle averaged over all the oxygen ions of the structure. With the exception of the small Be^{2+} and B^{3+} ions, all the other M–O bonds examined are considerably longer than the Si–O or Al–O of the host framework. The inclusion of the dopants in the framework will therefore induce a structural strain. The local tetrahedral environment of the low valence dopants is very distorted. The structural distortion is dictated by the non-chemical equivalence of the four nearest-neighbor oxygens of the M ion, caused by the presence of the acid proton bonded to one oxygen. For each dopant, the M–O_H distance to the protonated oxygen is at least 0.15 Å longer than the three M–O_{1-3} to the non-protonated oxygens. This result is consistent with previous computational studies of the Al^{3+}/Si^{4+} defect in zeolites that, given its importance in heterogeneous catalysis, has been characterized with a variety of computational techniques, including isolated [74] and embedded [75,76] QM clusters, supercell techniques [77,78] and forcefield methods [79]. Jahn–Teller type distortions for open-shell dopant ions, if present, play only a minor role compared to the relaxation around the acid OH group.

The situation is different for the isovalent dopants, whose four nearest neighbor oxygens are chemically equivalent. The four M–O bond lengths of Ga^{3+} and Fe^{3+} ions in AlPO-34 shows differences of less than 0.02 Å, while for Cr, Co and especially Mn, the coordination is distorted by Jahn–Teller effects. While closed-shell low valence dopants are located in a distorted environment, closed-shell isovalent ions occupy a more regular crystalline position. The only exception to this rule is B^{3+} in AlPO-34, which is too small to retain the undistorted tetrahedral coordination of the Al sites. When comparing the M–O bond distances calculated in our work with the experimental values, we notice that the error is not uniform: the calculated M–O distance for the 2+ dopant ions in AlPOs is generally overestimated. Furthermore, the error for ions that are stable in only one oxidation state,

Table 5
Equilibrium M–O_n bond lengths (R, in Å) and T–O–T' angles (in degrees) for the M dopant ions investigated in chabasite and AlPO-34

Dopant	Bond distances						T–O–T' bond angles				Energy
	R (M–O_1)	R (M–O_2)	R (M–O_3)	R (M–O_H)	$\langle R \rangle$	R_{expt}	M–O_H–Si	M–O–Si	T–O–Si	Si–O–Si	
Trivalent dopant ions in chabasite											
B	1.36	1.36	1.38	2.48	1.64	1.37 [62]	143.34	154.70	149.24	148.83	
Al	1.68	1.69	1.69	1.90	1.74		127.98	147.59	148.48	148.57	
Ga	1.75	1.76	1.77	1.99	1.82	1.83 [63]	126.16	142.25	147.58	148.11	
Fe	1.82	1.83	1.84	2.07	1.89	1.89 [64]	123.63	141.89	147.25	147.78	
Co	1.78	1.78	1.83	2.05	1.86		125.81	144.36	147.72	148.08	
Mn	1.81	1.81	1.83	2.18	1.91		127.48	143.94	146.83	147.12	
Si	1.61	1.61	1.61	1.62	1.61	1.60 [65]		148.97	148.97	148.97	
	R (M–O_1)	R (M–O_2)	R (M–O_3)	R (M–O_4)	$\langle R \rangle$	R_{expt}		M–O–P	T–O–P	Al–O–P	ΔE_{III}
Trivalent dopant ions in AlPO-34											
B	1.46	1.48	1.53	1.55	1.50	1.47 [66]		151.34	150.13	149.89	
Ga	1.80	1.81	1.81	1.82	1.81	1.82 [67]		144.90	148.99	149.81	0.377
Cr	1.88	1.88	1.89	1.91	1.89			144.95	147.99	148.60	2.258
Mn	1.86	1.87	1.91	1.91	1.88	1.85 [20]		138.74	147.54	149.30	0.844
Fe	1.86	1.87	1.87	1.88	1.87	1.86 [18]		144.58	148.72	149.55	1.034
Co	1.83	1.84	1.85	1.86	1.84	1.89 [68]		141.44	147.53	148.75	0.980
Al	1.72	1.72	1.73	1.73	1.73	1.73 [45]		148.59	148.59	148.59	—
	R (M–O_1)	R (M–O_2)	R (M–O_3)	R (M–O_4)	$\langle R \rangle$	R_{expt}	M–O_H–P	M–O–P	T–O–P	Al–O–P	ΔE_{II}
Divalent dopant ions in AlPO-34											
Be	1.53	1.54	1.56	2.31	1.74		141.25	143.01	147.88	148.85	
Mg	1.85	1.87	1.91	2.08	1.93	1.94 [69]	132.41	138.69	147.17	148.86	3.067
Ca	2.17	2.19	2.24	2.41	2.25		126.05	127.84	142.61	144.96	4.351
Cr	1.99	2.03	2.04	2.36	2.11		127.50	124.89	143.92	147.72	3.576
Mn	2.01	2.02	2.04	2.26	2.08	2.02 [70]	127.81	130.91	145.06	147.89	3.660
Fe	1.97	1.98	1.99	2.19	2.01		128.97	131.93	145.77	148.54	3.508
Co	1.94	1.94	1.95	2.14	1.99	1.94 [68]	129.34	133.79	146.06	148.51	3.393
Ni	1.89	1.89	1.90	2.19	1.97	1.94 [71]	126.44	135.56	146.41	148.58	3.948
Zn	1.90	1.90	1.91	2.19	1.97	1.96 [72] 1.98 [73]	131.30	132.47	145.73	148.38	3.038
Sr	2.36	2.42	2.45	2.55	2.44		116.20	118.14	140.49	144.96	4.996

$\langle R \rangle$ is the average M–O bond distance from our calculations, R_{expt} from experiment (on metal-doped frameworks when available, or from closely related materials). The columns relative to the angles refer to: M–O_H–T angle on the protonated oxygen nearest neighbor to the dopant; M–O–T average angle on the four oxygens nearest neighbor to the dopant; T–O–Si and T–O–P average angle over all the oxygens in the structure; T–O–T average angle over all the oxygens in the structure that are not nearest neighbor to the dopant. For the doped AlPO materials, ΔE is the calculated insertion energy of the dopant in the framework (Eqs. (7) and (8) in the text).

such as Mg^{2+}, Ni^{2+} and Zn^{2+}, is within the experimental error of ± 0.02 Å associated with the EXAFS technique employed. Fe, Mn and Co ions, that are known experimentally to exist in both 2+ and 3+ oxidation states in the AlPO framework, instead, show a much larger difference from the experimental results, up to 0.06 Å for Mn^{2+}.

Experimental measurements concerning the reduced form of MeAlPO catalysts are often performed on the as-synthesized material; calcination to remove the organic template can in fact oxidize, at least partially, the dopants. The overestimation of the calculated, compared to the experimental, bond distance of Mn^{2+} and Co^{2+} ions, suggests that also in the as-synthesized MeAlPO structure some of the dopant ions are present in 3+ oxidation state, and a mixture of M^{2+} and M^{3+} is present in framework. Since the XAS data are element-specific, but cannot differentiate its oxidation state [17], the experimental results average the properties of all the dopants in the solid. A fraction of M ions in 3+ oxidation state causes a decrease of the M–O bond distances observed experimentally. Results of calculations similar to those reported here can effectively help us in determining the average oxidation state of the transition metal dopants in the catalysts, such as the MnAlPO materials discussed in Ref. [20].

Let us now consider the changes that occur in the M–O–T and T–O–T framework angles in the doped frameworks, from which we can obtain information on the structural distortion around the dopant, complementary to the M–O bond distances examined above. The deviation of the calculated T–O–T angles between

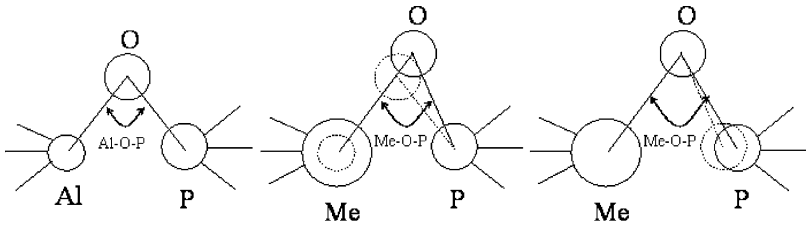

Fig. 5. Representation of the structural relaxation around a dopant in ALPO-34, and its effects on the M–O–T angles.

the doped and the undoped structure, in fact, provides a fast way to estimate the range of the structural distortion around the dopant. A representation of the relaxation is provided in Fig. 5; let us first imagine that, upon inclusion in the framework of the dopant, only its nearest neighbor oxygens are allowed to relax, while the next-nearest neighbor T ions and the rest of the structure are kept fixed (Fig. 5b). The larger the size of the dopant, the more its nearest neighbor oxygens will relax away from it. This relaxation movement causes a decrease of the M–O–T angles compared to the original T–O–T, proportional to the extent of structural relaxation. We have seen in the previous discussion that the M–O_H bond of low valence dopants to the protonated oxygen is longer than the other M–O bonds. Therefore we expect the M–O_H–T angle centred on the bridging hydroxyl group to be particularly small. Of course the real situation is more complex, and the structural relaxation extends beyond the nearest neighbors of the dopant. A radial relaxation of the next-nearest neighbor T ions, which is expected to follow the relaxation of the nearest neighbor oxygens, will cause the M–O–T angle to increase. As the relaxation extends to further shells of ions in the structure, also the T–O–T angles centred on oxygens further away from M will vary. However, since the crystalline matrix exerts a steric constraint on the metal dopant, the extent of structural relaxation decays when moving away from the dopant. The change in the bond angles between undoped and doped materials provides a numerical way to estimate the range of this structural relaxation: monitoring the change in the calculated bond angles for subsequent shells of neighbors, will enable us to estimate the region of the solid that is structurally affected by the dopant. Furthermore, it has been shown that the ^{31}P NMR chemical shift, i.e. a measurable observable, correlates with the average T–O–T' bond angle [80]. Understanding the correlation between the properties of the metal dopant, such as charge and ionic radius, with the local and long-ranged structural relaxation in a simple polymorph (chabasite and AlPO-34), and in an idealized situation of non-interacting defect centers, can provide a valuable reference against which to compare and rationalize the experimental information obtained for real MeAlPO catalysts.

The calculated values of the T–O–T angles for subsequent shells of neighbors of the metal dopants

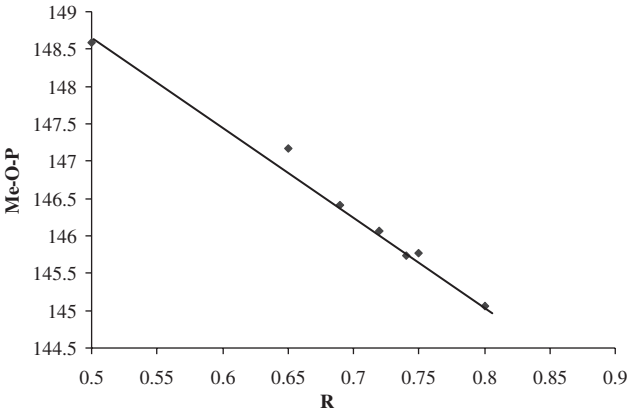

Fig. 6. Average value of the calculated M–O–P bond angle for divalent dopant ions in AlPO-34, as a function of the ionic radius of the dopant [84], R (in Å).

are reported in Table 5. Indeed, we find that the angular distortion from the undoped material is particularly pronounced around the protonated oxygen (column M–O_H–T), whose angle with the framework ions changes as much as 30° for the large Sr^{2+} dopant. The difference from the undoped framework is important for all the four nearest-neighbor oxygens of the dopant (column M–O–T); this local distortion causes a decrease of the T–O–T angle averaged over the whole structure. When we limit our attention to the oxygens not nearest neighbor of the dopant, however, we notice only minor changes (of less than 1°) from the undoped chabasite and AlPO-34 framework structures. This result suggests that the structural distortion caused by the dopant is "local", and affects its nearest neighbor ions, but does not propagate to the undoped regions of the framework. The only exceptions to the above result are Ca and Sr in AlPO-34, i.e. the largest dopant ions examined (see the M–O bond distances in Table 5). The value of the Al–O–P bond angles away from the Ca and Sr dopants are lower than the original value of the Al–O–P angle in the undoped AlPO-34, which indicates that the structural strain caused by the biggest dopant ions is long-ranged, and propagates towards the undoped region of the host framework. In Fig. 6 we plot the calculated value of the T–O–P angle for 2+ ions in AlPO-34, as a function of the ionic radius of the dopant. These two observables show good linear correlation, clearly

indicating that the structural distortion correlates with the steric hindrance of the large dopant ions when they are isomorphously introduced in the framework.

4.2. Chemical features of dopant ions in zeolites and AlPOs

To achieve a chemical characterization of the dopant ions, we have performed a population analysis of their bonding with the nearest oxygens, similar to that employed in Section 3.1 for the undoped frameworks. This result enables us to investigate the nature of the bonding of the metal dopants to the framework. Results are reported in Table 6, while electron density plots are shown in Figs. 7 and 8. All the open-shell transition metal ions investigated in our work are stable in the spin state with the highest multiplicity compatible with their count of d electrons. This high spin state would be expected, owing to the low crystal field splitting caused by the tetrahedral coordination of the transition metal ions. The partially covalent character of the P–O and Si–O bonds, discussed in Section 3, decreases the net charge of the oxygens, and makes the crystal field they create insufficient to stabilize low spin states on the transition metals. A higher crystal field splitting is required to stabilize a pairing of the d electrons. All the HF calculations reported in the following discussion are therefore based on transition metal ions in high spin configuration.

The calculated net charge of all the dopants studied are similar to their formal values, while the bonds between dopant and neighboring oxygens have low overlap population $Q_b(M-O)$. These features suggest that the bonding of the dopants to the host framework is ionic in nature, as was the case for the host Al^{3+} in

Table 6
Mulliken population analysis of the electronic distribution around the M dopant ions investigated in chabasite and AlPO-34

Dopant	$Q(M)$	$Q(O_{1-3})$	$Q(O_H)$	$Q(O_{1-4})$	$Q_b(M–O)$
Trivalent dopant ions in chabasite					
B	1.21	−0.92	−0.87	−0.91	0.26
Al	2.11	−1.15	−0.96	−1.10	0.13
Ga	2.28	−1.20	−0.98	−1.15	0.11
Fe	2.15	−1.15	−0.95	−1.10	0.11
Co	2.11	−1.15	−0.95	−1.10	0.11
Mn	2.01	−1.11	−0.91	−1.06	0.09
Si	2.06			−1.03	0.29
Trivalent dopant ions in AlPO-34					
B	1.57			−1.13	0.22
Ga	2.33			−1.26	0.11
Cr	2.15			−1.24	0.08
Mn	2.17			−1.24	0.09
Fe	2.23			−1.26	0.10
Co	2.20			−1.26	0.10
Al	2.19			−1.26	0.14
Divalent dopant ions in AlPO-34					
Be	1.75	−1.33	−0.99	−1.24	0.03
Mg	1.67	−1.26	−1.03	−1.20	0.05
Ca	1.78	−1.25	−1.01	−1.19	0.00
Cr	1.60	−1.22	−0.98	−1.17	0.04
Mn	1.54	−1.21	−0.99	−1.16	0.05
Fe	1.62	−1.24	−1.01	−1.18	0.06
Co	1.61	−1.24	−1.01	−1.18	0.07
Ni	1.85	−1.32	−1.03	−1.24	−0.01
Zn	1.42	−1.20	−0.98	−1.15	0.09
Sr	1.84	−1.25	−1.01	−1.19	−0.02

The symbol Q refers to the net ionic charges on the metal dopant and oxygens; $Q(O_{1-3})$ is the average net charge of the three unprotonated oxygens that are nearest neighbor to M; Q (O_H) is the charge of the protonated oxygen, Q_b denotes the average M–O bond population, in $|e|$.

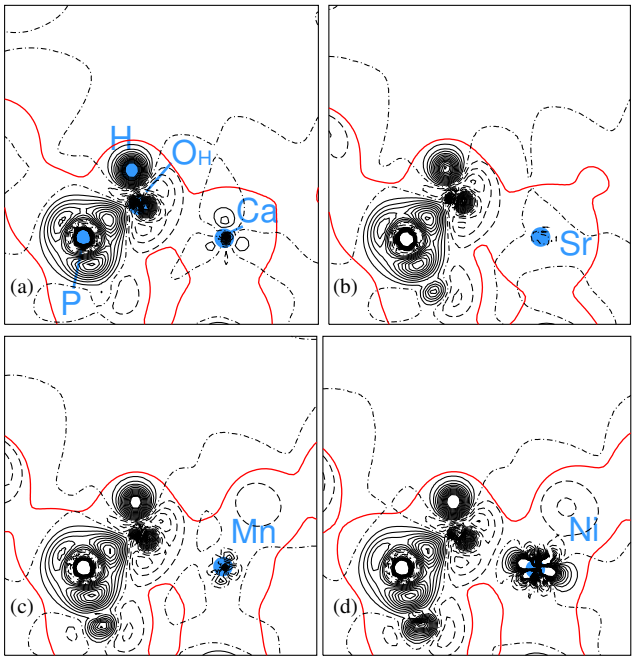

Fig. 7. Difference electron density maps (solid minus isolated formal ions) for 2+ dopant ions in AlPO-34, plotted in a plane containing one (a) Ca–O_h–P, (b) Sr–O_h–P, (c) Mn–O_h–P, or (d) Ni–O_h–P unit. Continuous and dashed lines correspond to positive and negative densities, plotted between −0.1 and 0.1 au ($|e|$ bohr^{-3}) at linear steps of 0.01 au. The thicker line is the total electron density level of 0.01 au and indicates the framework size.

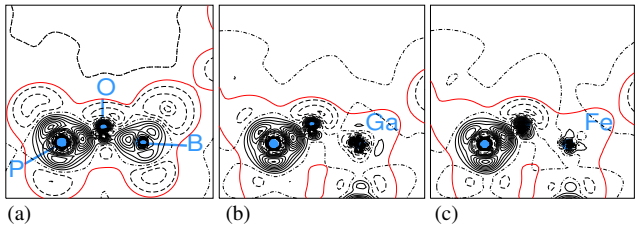

Fig. 8. Difference electron density maps (solid minus isolated formal ions) for 3+ dopant ions in AlPO-34, plotted in a plane containing one B–O–P (a), Ga–O–P (b) or Fe–O–P (c) unit. Symbols and units as in Fig. 7.

AlPOs (see Section 3.1). Only B^{3+} has a different behavior, with a low net ionic charge and a high overlap population, suggesting that B^{3+} bonds covalently to the neighboring oxygens. This result is not surprising as B^{3+} is a small ion and is more electronegative than Al^{3+} and the other dopants. To support this finding, in Figs. 7 and 8 we show the electron density maps (obtained as the difference between the electron density in the solid and the superposition of isolated formal ions) for the *M*–O bond in a selection of metal-doped AlPO-34 frameworks. The maps are drawn in a plane containing the dopant, one nearest oxygen (O_H for the 2+ dopants), and the next nearest P ion bonded to the oxygen of the figure. In the electron density plots we see only minor features around the metal dopants; again B^{3+} behaves differently, and causes a significant electronic redistribution. Experimental TGA data on doped AlPO materials show that the hydrophilicity of the framework increases when dopant ions are incorporated [18,81], a result that is consistent with the ionic nature of the *M*–O bonding found in our calculations.

4.3. Substitutional energy of dopant ions in microporous AlPOs

The feasibility of the isomorphous substitution of different dopants, and the structural stability of the doped materials, depend crucially on the thermodynamic stability of the dopant ions in the framework. To understand this topic, we have calculated the energetics of low valence and isovalent ions in the Al framework site of AlPO-34. We have chosen the AlPO-34 framework for this part of our study, as AlPOs show a greater flexibility than zeolites towards chemical substitutions.

The synthesis of MeAlPOs is usually performed in an aqueous medium, by hydrothermal methods [1]; we shall therefore consider the following reactions for the inclusion of the 2+ and 3+ dopants in the AlPO framework:

$$\text{ALPO-34} + [M^{II}(H_2O)_6]^{2+} \xrightarrow{\Delta E_{II}} M^{II}\text{HAlPO-34} + [Al(H_2O)_5(OH)]^{2+}, \quad (5)$$

$$\text{ALPO-34} + [M^{III}(H_2O)_6]^{3+} \xrightarrow{\Delta E_{III}} M^{III}\text{AlPO-34} + [Al(H_2O)_6]^{3+}, \quad (6)$$

which correspond to a replacement energy of di- and trivalent dopants defined as follows:

$$\Delta E_{II} = E[Al(H_2O)_5(OH)]^{2+} + E(M^{II}\text{HAlPO-34}) - E(\text{ALPO-34}) - E[M^{II}(H_2O)_6]^{2+}, \quad (7)$$

$$\Delta E_{III} = E[Al(H_2O)_6]^{3+} + E(M^{III}\text{AlPO-34}) - E(\text{ALPO-34}) - E(M^{III}(H_2O_6)]^{3+}. \quad (8)$$

We have taken as suitable states for the +2 and +3 metal ions outside the framework their hexa-aqua complexes $[M(H_2O)_6]^{n+}$. Of course, this representation of the hydrated ions is an approximation, as only the first solvation sphere is included; nonetheless, it represents a suitably simple computational model of the solvated ions. The $[Al(H_2O)_5\ (OH)]^{2+}$ complex in reaction (1) is required to charge-balance the inclusion of a 2+ dopant. Since the $[Al(H_2O)_5\ (OH)]^{2+}$ species is unstable, we consider as reliable only the trends in the calculated replacement energy ΔE_{II}, and not its absolute value. The values of ΔE_{II} and ΔE_{III} indicate the relative energetic stability of the different *M* dopants examined in the AlPO framework during the synthesis.

We have performed a geometry optimization of both the molecular and solid systems with a consistent set of computational parameters. The calculated values of ΔE_{II} and ΔE_{III} for the dopant ions investigated are summarized in the last column of Table 5 (the small Be^{2+} and B^{3+} ions are excluded, as the $[M(H_2O)_6]^{n+}$ complex employed in Eqs. (7) and (8) is unsuitable to represent these hydrated ions). The calculated values of ΔE_{II} and ΔE_{III} are reported in Fig. 9 as a function of the average *M*–O bond distance in the equilibrium structure. The latter value is of course closely related to the ionic radius of the dopant. For the 2+ ions, the longer *M*–O_H distance with the protonated oxygen is excluded from the average. The ionic size of the dopants has a clear influence on their stability in the framework, and the replacement energy increases linearly as a function of the *M*–O bond distance. Ni^{II} and Cr^{III} do not follow the linear trend in the calculated value of ΔE as a function of their ionic size. This result is to be attributed to the instability of transition metal ions with electronic configuration $d^{(3)}$ (Cr^{III}) and $d^{(8)}$ (Ni^{II}) in tetrahedral coordination. The crystal field stabilization energy of octahedral and tetrahedral Cr^{III} and Ni^{II} ions has been estimated for oxides with the spinel structure [82]. The resulting values are 1.226 eV for octahedral Ni^{II}, 0.372 eV for tetrahedral Ni^{II}, 2.33 eV for octahedral Cr^{III} and 0.69 eV for tetrahedral Cr^{III}, with a difference of 0.854 eV for Ni^{II} and of 1.64 eV for Cr^{III}. These values, when subtracted from the values of ΔE_{II} and ΔE_{III} calculated here, would bring the replacement energy of Ni^{II} and Cr^{III} ions in-line with the behavior shown by the other 2+ and 3+ dopants. We expect therefore the substitution of Cr^{III} and Ni^{II} ions in the tetrahedral sites of AlPOs to be of difficult accomplishment, as confirmed by experimental evidence, which shows that the amount of Ni that can be incorporated in AlPOs is relatively low compared to other divalent metal ions [13].

The linear trend in the values of ΔE_{II} and ΔE_{III} as a function of the ionic radius of the dopant has a clear structural explanation. As discussed in Section 4.1, the *M*–O bond distances are longer than those of the Al–O

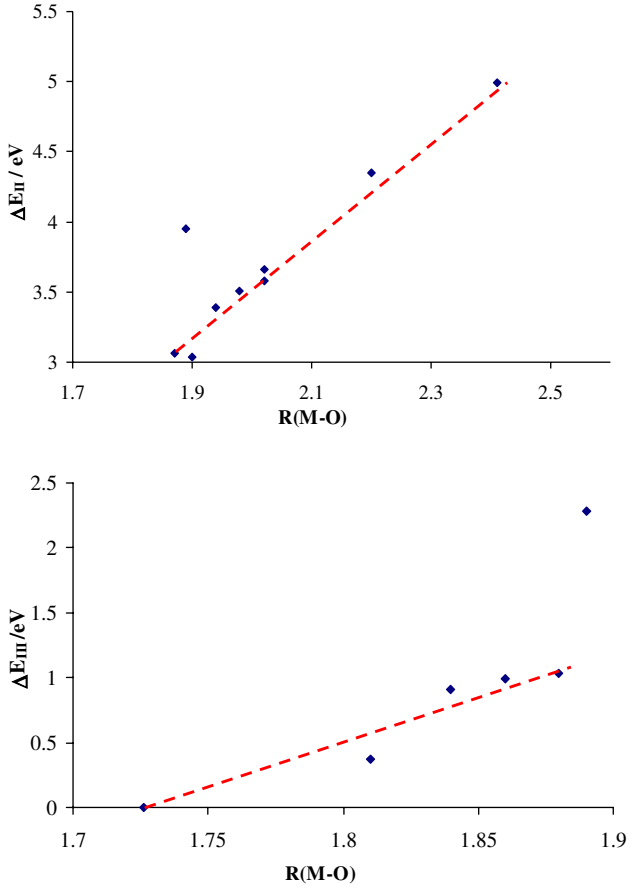

Fig. 9. Calculated replacement energies ΔE_{II} and ΔE_{III} (in eV) as a function of the average M–O bond distance $R(M$–O), in Å, for divalent and trivalent dopant ions in AlPO-34.

bonds they replace. The AlPO structure compromises locally the steric strain introduced by the larger dopant ion by bending the (flexible) M–O–P angles centered on its nearest neighbor oxygens. The calculated value of the M–O–P angle in the equilibrium structure (see Fig. 6) shows a linear relationship when plotted as a function of the size of the dopant ion. Given the linear relationship of both M–O–P angle and replacement energy as a function of the ionic size of the dopant, we attribute the trend shown in Fig. 9 for the energetics of the framework doping, to the structural distortion around the dopant, which destabilizes the doped structure.

4.4. Site ordering of dopant ions in microporous AlPOs—size effects

Most zeolite and AlPO frameworks have a complex structure, with several non-symmetry equivalent T sites. Not only the possibility of including dopant ions in the framework is of interest, but also the type of incorporation. This can occur in either ordered or disordered fashion. The former case, in which the dopant shows a marked preference for a specific T site of the structure, should be preferred for applications in catalysis; all active centers would in fact be located in the same crystalline environment, thus enhancing the selectivity of the catalyst. A disordered replacement in different T sites would locate the dopants in different environments, a feature that can contribute to decreasing the selectivity. We would therefore like to understand the factors that promote site ordering.

If the inclusion of the dopant is at least partially thermodynamically controlled, the degree of ordering of the dopant can be examined in a computational study by calculating the relative replacement energy of the dopant ion in the different T sites of the framework under investigation. A range of replacement energies comparable to the thermal energy will result in disordered distribution across T sites, while a range of replacement energies greater than the thermal energy indicates a strong preference of the dopant towards an ordered incorporation in the framework.

As we have seen in Sections 4.1–4.3, the ionic radius of the dopant controls its structural features and the energetics of the inclusion in the framework. Furthermore, the cation size has a major effect upon the site distribution in spinels [83], where octahedral and tetrahedral sites are available. All the framework sites in zeotypes are tetrahedrally coordinated and are differentiated only by the number of second or further shells of neighbors of the dopant. In such a case, the chemical interaction between dopant and nearest neighbor oxygen ions is largely equivalent in different polymorphic structures, as shown by the results of Section 3; the ease of inclusion of the dopant is related to the topology of the host framework, and the ease with which it can adapt to the incorporation of ions of variable size.

To investigate this topic, we have studied with IP techniques the structure and energy of trivalent substitutional ions of different size, which replace a framework Al in two different AlPO polymorphs, namely AlPO-41 (AFO) and DAF-1 (DFO), shown in Fig. 10. These two frameworks have a variety of topologically different T sites, incorporated into rings ranging in size from 4 to 12 tetrahedra, thus enabling us to examine the combined effect of dopant size and framework topology onto the dopant ordering.

As described in Section 2, we modified the effective size of the dopant ions by varying the pre-exponential factor of their Buckingham potential. In our work we assumed the ionic radius of the framework Al^{3+} to be $R_{Al} = 0.51$ Å [84], and examined a range of ionic radii for the dopant ions M of $0.35\,\text{Å} < R_M < 0.90\,\text{Å}$, which covers most of the $3+$ ions in the periodic table.

For each dopant size R, we located one substitutional dopant in each unit cell of the host framework, composed of 10 formula units in AFO, and 132 formula units in DFO; we examined the dopant incorporation

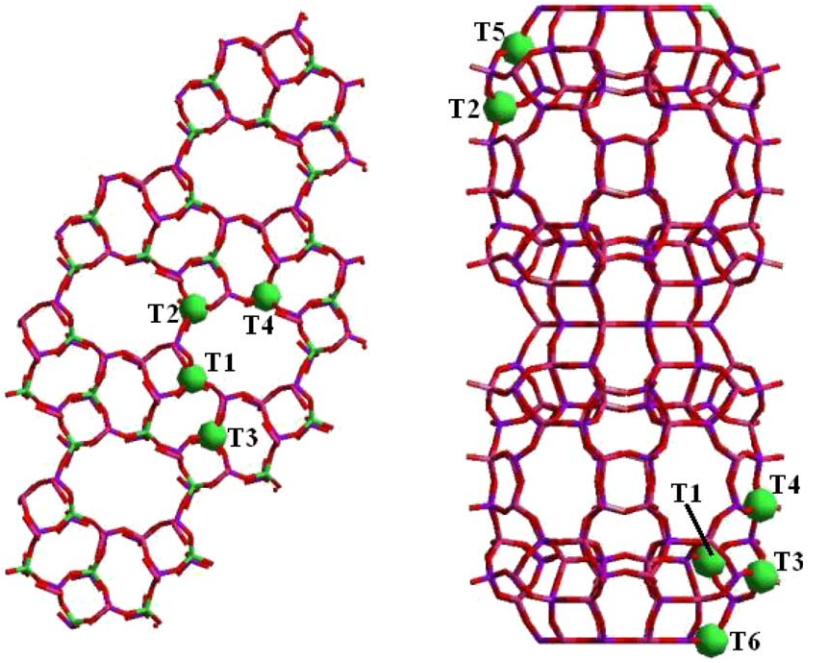

Fig. 10. Framework topology of AFO (left) and DFO (right) AlPO structures, with the topologically non-equivalent T sites labeled according to the Atlas of zeolite framework types [56].

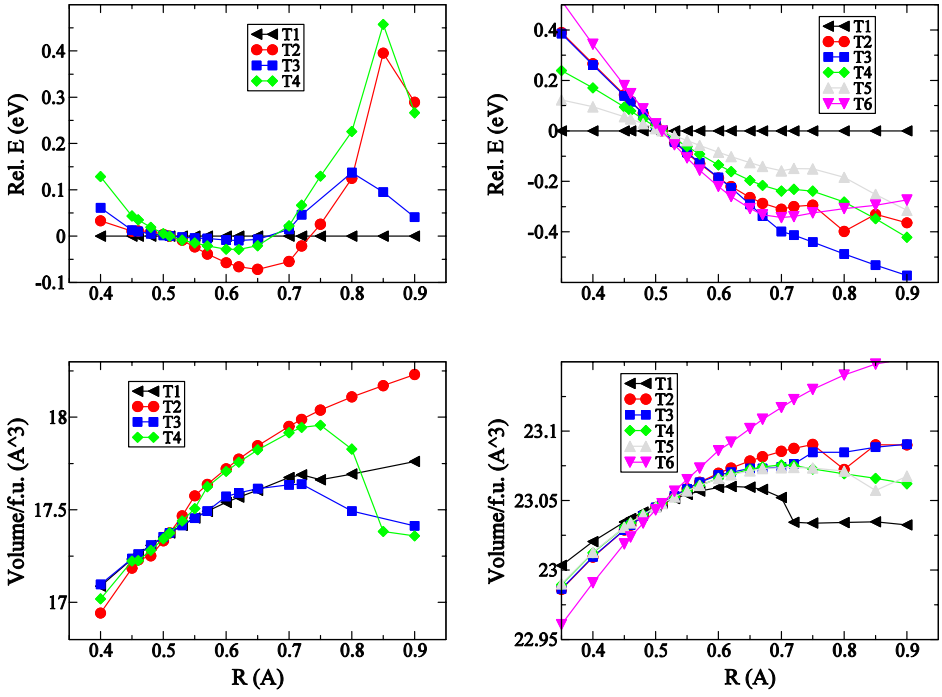

Fig. 11. Relative replacement energy ΔE_n (eV/dopant), and volume per formula unit V_n (Å^3) for the doped AFO (left) and DFO (right) frameworks, as a function of the dopant radius R (Å).

in each topologically unique T site, T_n (4 in AFO and 6 in DFO). In the following discussion, sites are labeled as in the Atlas of zeolite framework types [56] (labels are also reported in Fig. 10). For each combination of dopant size and T site, we have fully relaxed the structure to minimum energy, using $P1$ symmetry. In Fig. 11 we report the relative energies of the doped frameworks and the equilibrium volume per formula unit, against the ionic radius R of the metal dopant. The relative lattice energies (ΔE_n) are calculated, for each

value of R, by taking the energy of the stable site T_i for the smallest ions ($T1$ both in AFO and DFO) as reference, i.e. $\Delta E_n(R) = E_n(R) - E_1(R)$.

We see in Fig. 11 that the relative lattice energies $\Delta E_n(R)$ are small for values of R similar to R_{Al} ($\Delta E_n(R_{Al}) = 0$ by necessity, as this is the undoped AlPO framework). The more R deviates from R_{Al}, the larger the energy dispersion of the ΔE_n values. This result indicates that a site-ordered inclusion in the framework is energetically favored for dopant ions whose size is most different from that of the host Al^{3+} ion they replace. Ions of similar size to Al would instead favor a disordered inclusion into the AlPO framework. To rationalize this behavior we examine how the local environment of the dopant ion changes with the ionic size R. In the AFO framework, ions smaller than Al are stable in site $T1$, whereas dopant ions bigger than Al are energetically stable in site $T2$. The biggest change in the lattice energy and volume as a function of the ionic radius is seen for site $T2$, whereas for $T1$ (and $T3$) we see a small change in the energy and cell volume as the ionic size of the metal dopant varies. We observe a similar behavior for the DFO framework, in which site $T6$ shows the biggest change in both energy and cell volume as the ionic size of the metal dopant increases; sites $T6$ and $T3$ are energetically stable for ions that are bigger than Al. The smallest change of the energy and cell volume is seen for site $T1$, which is stable for dopants that are smaller than Al.

This behavior can be rationalized by partitioning the framework T sites into two structural types:

(1) *Caged T sites*, which include $T1$ and $T3$ in AFO; $T1, T4$ and $T5$ in DFO. The framework forms a rigid structure around the site, with strong structural constraints. The framework structure around the 'caged' T sites is not free to relax upon doping; in particular its next-nearest neighbor P sites cannot readily relax outwards following the dopant incorporation. The main relaxation movement around large dopants is therefore a bending of the Me–O–P angles around its nearest-neighbor oxygens, which decrease on increasing R. Since the relaxation is local around the dopant, it causes only minor changes in the cell volume as a function of R, and the replacement of large ions is energetically unstable.

(2) *Free T sites*: This is the case of $T2$ in AFO and $T6$ in DFO, which are part of a large ring system, and hence are located in a more flexible framework region. The framework topology allows larger portions of the structure to relax around the dopant, which is reflected in the larger increase of the cell volume of the doped framework as a function of R. Since there are fewer structural constraints, replacement of large dopant ions is energetically favorable in the 'free' T sites.

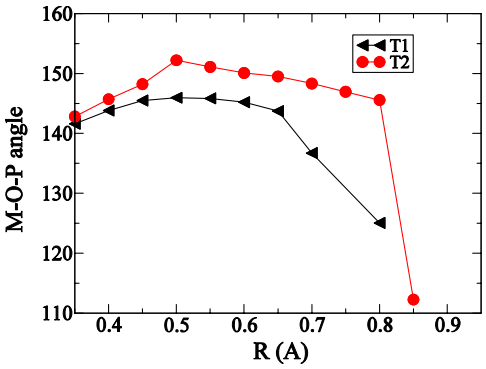

Fig. 12. Variation of the M–O–P bond angle (averaged over the four oxygens that are nearest neighbor to the dopant M) as a function of the dopant radius R (Å), for sites $T1$ (caged) and $T2$ (free) in AFO.

The different structural behavior is clearly illustrated in Fig. 12, where we report the equilibrium value of the M–O–P angle (averaged over the four oxygens that are nearest neighbor to the dopant) for sites $T2$ (free) and $T1$ (caged) in AFO. The value of the M–O–P angle is smaller in the latter case, indicative of a more strained structure around the dopant (see the discussion in Section 4.1). The structural freedom of the T sites is not unlimited: even if the substitution occurs in the more flexible T sites, on increasing the size of the metal dopant the structure becomes more and more rigid, until it swaps to a caged T site behavior. This feature is illustrated by the progressive decrease of the M–O–P angle around site $T2$ in Fig. 12, which collapses for the largest dopant ions examined.

This result indicates that the size of metal dopants has a major influence upon their site ordering. Bigger metal dopants, although of more difficult inclusion in the framework, prefer to substitute 'free' Al sites, located in unconstrained regions of the framework, whereas small metal dopants are energetically stable when replacing Al sites situated in smaller cages. This site preference increases on increasing the size difference between host ion and dopant, and is explained via the topological features of the host framework.

4.5. Influence of the counterion on the local environment and electronic structure of the active sites

Zeotype frameworks can be modified in post-synthetic treatments; for instance, the extraframework ions charge-balancing the presence of low valence dopants can be modified by ion-exchange operations, and the acid protons replaced by larger inorganic cations, such as Na^+, K^+ or polyvalent ions. The crystalline environment of the active sites is modified during this operation, introducing an additional way to influence the structural and electronic properties of the dopant ions, and hence also the catalytic activity. Understanding

Table 7
Equilibrium bond distance(s) R_n, in Å, between the counterions examined and the framework oxygens, in order of increasing bond distance

Ion	H		Li		Na		K	
Dopant	Al^{3+}	Fe^{3+}	Al^{3+}	Fe^{3+}	Al^{3+}	Fe^{3+}	Al^{3+}	Fe^{3+}
R_1	0.949*	0.948*	1.921*	1.838*	2.286*	2.304*	2.769*	2.746*
R_2			2.061*	1.896*	2.549	2.345*	3.064	3.096*
R_3			2.380		2.662	2.702	3.158*	3.189
R_4							3.171	3.198
R_5							3.299	3.255
R_6							3.361	3.297
R_7							3.509	3.427

Numbers marked with the symbol * refer to the oxygens that are nearest neighbor to the dopant ion.

Table 8
Equilibrium bond distances R_n, in Å, between the dopant and its four framework oxygen neighbors, in order of increasing bond distance

	R_1	R_2	R_3	R_4	$\langle R \rangle$
Al^{3+}					
H	1.6787	1.6902	1.6974	1.8994*	1.7414
Li	1.6972	1.6988	1.7310*	1.7907*	1.7290
Na	1.6975	1.7066	1.7278	1.7672*	1.7248
K	1.6993	1.7182	1.7230	1.7486*	1.7223
AlPO	1.7195	1.7229	1.7287	1.7334	1.7261
Fe^{3+}					
H	1.8222	1.8282	1.8358	2.0660*	1.8880
Li	1.8270	1.8364	1.9024*	1.9367*	1.8756
Na	1.8314	1.8497	1.8744*	1.9161*	1.8679
K	1.8446	1.8651	1.8666	1.9011*	1.8693
FAPO	1.8649	1.8654	1.8678	1.8808	1.8697

$\langle R \rangle$ indicates the average of the four bond distances R_{1-4}. Numbers marked with the symbol * refer to the oxygens closely associated with the counterion.

how the chemistry of the dopants is influenced by the counterion is another step towards controlling the catalytic activity and selectivity of these heterogeneous catalysts. To this aim, we have investigated with QM methods how different counterions affect the structure and chemistry of Al^{3+} and Fe^{3+} ions in the framework of chabasite and AlPO-34. In the zeolite framework, the Al^{3+} and Fe^{3+} ions have been charge-balanced in our calculations by protonating one of the framework oxygens nearest neighbors of the dopant, or by adding one Li, Na or K extraframework ion. It is also of interest to compare the local structure of the 3+ metal ions in zeolites with that in AlPOs, where the 3+ ions are isovalent (the host ion itself in the case of Al), and hence do not require charge compensation. The Lewis acidity of an ion with charge Q and radius R scales as Q/R^2 [85]; in this view, the non-counterion situation of AlPOs can be considered as equivalent to a counterion of charge +1 and of infinite size. The charge-balancing ions examined here span therefore the complete range of ionic sizes, from the smallest counter cation (H), to extraframework ions of increasing size (Li, Na, K), to the non-counterion situation in AlPO-34. Examining the local structural environment of Al^{3+} and Fe^{3+} ions in chabasite and AlPO-34 enables us to investigate how much the presence and type of counterion can influence the structural and electronic properties of the dopant.

The calculated equilibrium structure, for each combination of dopant and counterion is reported in Tables 7 and 8. The equilibrium structure for the Fe^{3+} dopant in chabasite with Li, Na and K counterions is also shown in Fig. 13. Let us first consider how the size of the counterion affects its interaction with the framework oxygens. In Table 7 we list the calculated equilibrium bond distances between the counterions and the framework oxygens, in order of increasing distance; the values marked with a symbol (*) refer to the oxygen atoms nearest neighbors of the dopant. H has an obvious association with only 1 oxygen, the one to which it is covalently bonded to form the OH Brønsted acid site. The other extraframework ions have an ionic type of interaction with the framework oxygens, and are effectively "solvated" by the zeolitic framework. They show a marked association with two or more framework oxygens, depending on the relative size of the counterion compared to the interstices available in the microporous

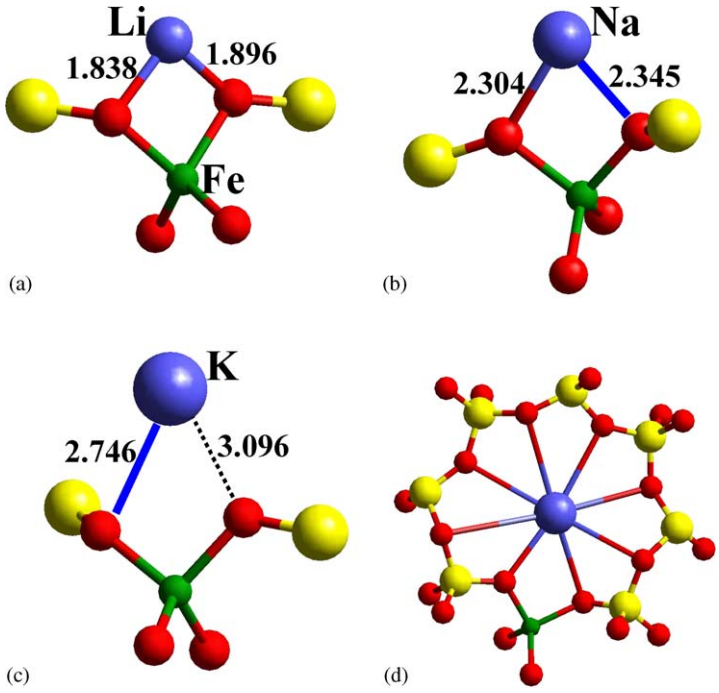

Fig. 13. Equilibrium structure of (a) Li^+, (b) Na^+ and (c) K^+ counterions next to a Fe^{3+} substitutional dopant in chabasite. (d) Equilibrium position of the K^+ ion, highlighting its location near the center of one eight-membered ring of tetrahedra of the chabasite structure.

zeotypic structure; in the same zeolite type, it increases on increasing the ionic size of the extraframework ion. The small Li^+ ions are located in a bridging position between two oxygens, both nearest neighbors of the Al or Fe dopant, with similar but not equal Li–O bond distances. The larger Na^+ ions, when located next to an Al dopant, increase their coordination number to the framework oxygens to 3, of which only one is nearest neighbor of the Al dopant. The shortest Na–O bond length, of 2.286 Å, is achieved with the latter oxygen, while the other two are $\sim$0.3 Å longer. The local structure of Na^+ calculated here, is similar to that of the ion labeled as Na5 in site III′ in the experimental work on the NaX zeolite [86]. When Na^+ is next to an Fe^{3+} dopant, which is larger than Al^{3+} (compare the Al–O and Fe–O bond distances in Table 8), the spacing between the oxygens nearest neighbors to Fe increases and appears to be of optimal size to host the extraframework Na^+. The Na^+ ion in Fe-doped chabasite, therefore, has two short and one long bond distances with the framework oxygens. The even larger K^+ ions, finally, are located close to the center of eight-membered rings, where they can interact with up to eight framework oxygens. This increase in coordination number of K^+ is achieved partially by weakening its association with the framework oxygens that are nearest neighbor to the dopant (for both Al and Fe ions), with which K^+ retains only one short bond. The location of extraframework Li, Na and K ions has been investigated computationally in other zeolitic framework types [87–92], all of which have different pore openings than the chabasite polymorph examined here. It is therefore difficult to compare, other than qualitatively, the local environment of the extraframework ions calculated here with previously published results. The trend relative to the increase of coordination number of the extraframework ion with its ionic size, found here in chabasite, is common to the offretite [87] and faujasite (X) [92] zeolitic structures, suggesting a general validity.

From a computational point of view, it is of interest to examine the counterion location calculated with different models of the active site. QM studies performed with models of the solid based on periodic boundary conditions [87,88,90], such as the one employed here, yield equilibrium structures in which the bond distances between extraframework ion and framework oxygens are different from each other; the same result is obtained experimentally [86]. Models of the active site based on isolated cluster techniques, instead, favor a structure in which the local environment of the extraframework ion is more symmetric, with distances from the framework oxygens more similar (or equal) to each other (see for instance [89]). We consider that the latter result highlights a limitation of cluster model studies; if not accurately chosen, the molecular fragment employed to represent the zeolitic framework is under-constrained, and it can adapt too easily to the extraframework ion, thus yielding an equilibrium structure in which the distance of each framework oxygen from the extraframework cation is individually optimized (and thus equal). This is not the case in the true (extended) solid, where the equilibrium location of

Table 9
Electronic distribution, measured via a Mulliken population analysis, of the Al^{3+} and Fe^{3+} dopant ions in chabasite and AlPO-34 as a function of the counterion

Dopant/counterion	Q_M	Q_{b1}	Q_{b2}	Q_{b3}	Q_{b4}	Q_{T4}	Q'_{b4}	Q_{T1}	Q'_{b1}
Al^{3+}									
H	2.113	0.178	0.171	0.173	0.076*	2.035	0.183	2.006	0.360
Li	2.119	0.165	0.161	0.153*	0.118*	1.971	0.311	2.001	0.377
Na	2.118	0.164	0.155	0.152	0.127*	1.977	0.333	1.997	0.379
K	2.114	0.162	0.148	0.153	0.137*	2.030	0.350	1.997	0.380
AlPO	2.191	0.139	0.139	0.139	0.136				
Fe^{3+}									
H	2.146	0.135	0.123	0.127	0.050*	2.029	0.197	2.017	0.366
Li	2.131	0.132	0.125	0.096*	0.091*	1.986	0.318	2.011	0.371
Na	2.131	0.125	0.119	0.101*	0.097*	1.987	0.341	2.007	0.380
K	2.134	0.124	0.107	0.114	0.100*	1.978	0.356	2.011	0.384
FAPO	2.230	0.100	0.100	0.099	0.099				

The symbols used are illustrated in Fig. 15a, and refer to: net charge of the dopant (Q_M); bond population of the dopant with the four oxygen neighbors Q_{bn}; bond population of the oxygens O_1 and O_4 (those with the shortest and longest M–O distance) with their neighbor Si ion of the host framework in chabasite (Q'_{bn}), and net charge (Q_{Tn}) of these two Si ions. Charges are measured in $|e|$. The values marked with a * refer to the oxygens in close association with the counterion. The corresponding values of Q_T and Q'_b in undoped chabasite are 2.03 and $0.29|e|$.

the extraframework ion is due to a compromise between the highest coordination number and the strength of its interaction with each framework oxygen. Periodic models reproduce correctly this behavior.

Our calculations suggest that the type and location of the extraframework ion can modify the structural (Table 8) and electronic (Table 9) properties of the framework oxygens and of the dopant ions (M). By analyzing the data of Table 8, we find that those O ion(s) that are in closer contact with the counterion (marked with a symbol (*) inTables 8 and 9) have M–O bonds that are sizeably longer than those of the oxygens not closely associated to the counterion. The influence of the counterion on the framework oxygens scales inversely with the size of the counterion. The Al–O_H bond length of the dopant Al with the protonated oxygen in chabasite is 0.208 Å longer than (the average of) the other three Al–O distances. The difference (Δd) in the Al–O bond distance of the Al dopant with the oxygen(s) associated and not with the counterion decreases to 0.082, 0.057 and 0.035 Å for the Li, Na and K counterions, respectively. The same values are of 0.237, 0.088, 0.079 and 0.042 Å for the Fe dopant, charge balanced with H, Li, Na and K ions, respectively. The structural anisotropy around the dopant with the K^+ counterion is similar to the non-counterion situation seen in AlPO-34, where the difference between the longest M–O bond and the average of the other three is 0.010 Å for Al and 0.021 Å for Fe^{3+}. If we take the parameter Δd as being representative of the effect of the extraframework ion on the structure of the dopant (active site) in the framework, and plot Δd as a function of the ionic size R (see Fig. 14), the correlation between the ion type and the structural distortion it introduces in the framework is evident: the smaller the size of the

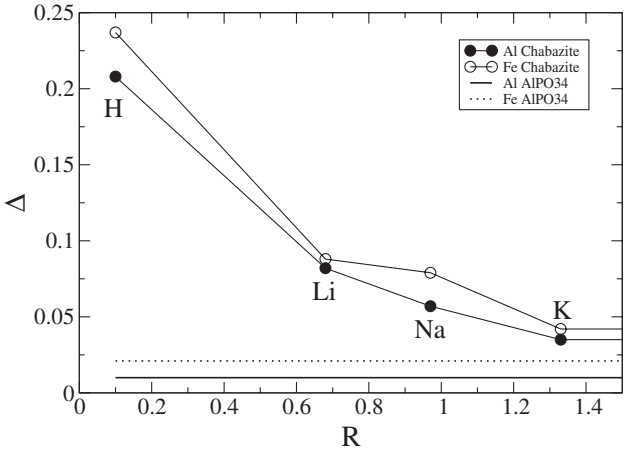

Fig. 14. Effect of different counterions on the structure of the dopant in chabasite and AlPO-34. Δd is the structural anisotropy in the coordination environment of the dopant, defined in the text; R the ionic size of the counterion [84], in Å. Filled and empty symbols refer to the Al^{3+} and Fe^{3+} dopant ions, respectively.

extraframework ion, the larger its effect on the framework structure. This result is in qualitative agreement with the Lewis acid strength of the extraframework ion, QR^{-2} proposed in Ref. [85]. For the experimental characterization of catalysts, it is of interest to notice that the association of the counterion with one or more of the framework oxygens alters substantially the individual M–O bond distances in the framework, and hence also the local symmetry of the dopant M, but not the value of the M–O distance averaged over the four M–O bonds of its tetrahedral environment. Moreover, for both Al^{3+} and Fe^{3+} ions, the average M–O bond distance in AlPO-34 is the same as in chabasite, and is therefore dictated by the ionic radius of the dopant, and

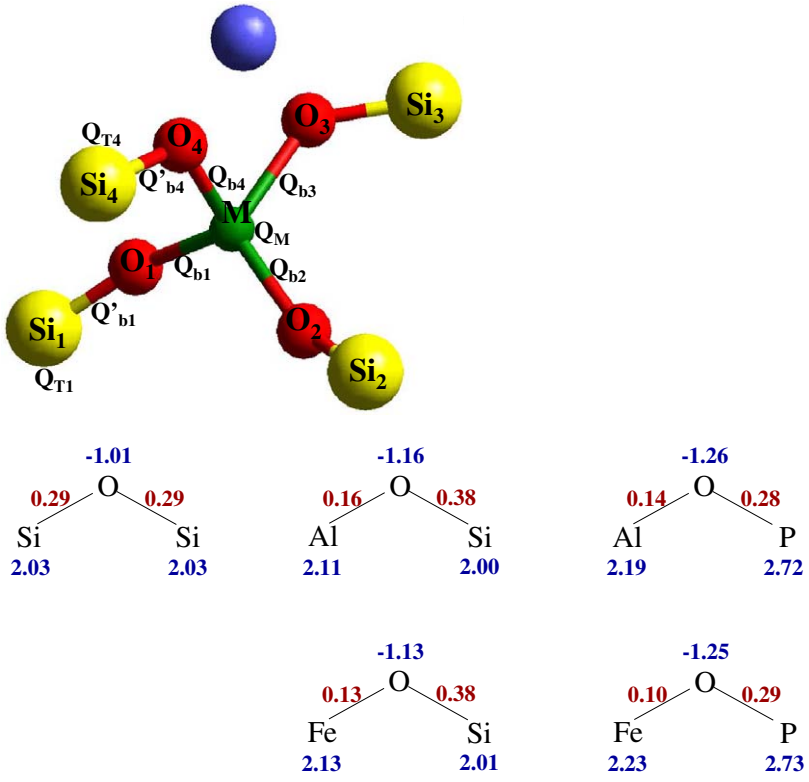

Fig. 15. (a) Explanation of the symbols used in Table 9; (b) electronic distribution, measured via a Mulliken population analysis, of the framework ions in pure and doped chabasite and AlPO-34. The values refer to net atomic charges and bond populations, measured in $|e|$.

not by its crystalline environment. Experimental values of the bond distances obtained from EXAFS data, especially when they are fitted using four M–O bonds of the same length (as is often the case), are therefore transferable among different counterions.

The counterion affects also the bonding character of the dopant to the framework ions. Results analyzing this feature are summarized in Table 9 and Fig. 15, where we report the net charge of the dopant (Q_M), and its bond population with the four oxygen neighbors Q_{bn}. We also report the bond population Q'_{bn} of the oxygens O_1 and O_4 (those with the shortest and longest M–O distance) with their neighbor Si ion of the host framework in chabasite, and the net charge (Q_T) of these two Si ions. The values of the net and bond charges reported in Table 9 enable us to extend the chemical characterization of the dopant ions given in Section 4.2. Our results indicate that when a framework oxygen is located between two cations of different formal charges, it forms a covalent bond with the neighbor with higher charge, and an ionic bond with the neighbor with lower charge. The larger the charge difference between the two T sites bonded to the same oxygen, the larger the difference in the nature of the two T–O bonds. We have shown in Section 3 that in pure AlPOs the P–O bonds are covalent, while the Al–O bonds are ionic. The framework oxygens next to the undervalent dopant in chabasite are bonded to one 3+ and one 4+ atoms; they react to this charge inequivalence of their two neighbors by bonding more covalently to the framework Si. The Si–O bond population increases from $0.29|e|$ in the undoped chabasite framework to $\sim 0.38|e|$ for the Si atom bonded to O_1. At the same time, the net charge of the silicons that are next-nearest neighbor to the 3+ dopant decreases, confirming a more covalent nature of their bonding with the oxygens. If we further consider the bonding of the dopant with its nearest oxygens, we see that both Al and Fe have higher values of Q_b in the zeolite framework than in AlPOs (the difference being of $\sim 0.03|e|$ in the bond to each oxygen that is not associated with the extraframework ions). As a result, the net positive charge of the dopant is higher in AlPO-34 than in chabasite. The above comparisons indicate that the oxygens in the framework are more polarized towards P in AlPOs than towards Si in chabasite; ionic metal dopants increase the covalence of the framework in the neighboring region. We expect this feature to influence the chemical and catalytic behavior of the dopant; in particular its Lewis acidity, which is linked to the ionicity of the M–O bonds.

5. Catalytic properties of doped zeotypes

After the electronic and structural characterization of the doped frameworks, we shall now investigate three

properties of the dopant ions that are of direct interest for their catalytic behavior. These are the Brønsted and Lewis acid strength, and the redox potential, which are examined separately in the following of the discussion.

5.1. Brønsted acid strength of low valence dopant ions in microporous zeolites and AlPOs

Several doped zeolites and AlPOs display solid acid behavior, of interest in heterogeneous catalysis [2,9]. Transformation reactions of methanol, i.e. the methanol to olefins (MTO) and methanol to gasoline (MTG) processes, are typical acid-catalyzed reactions that exploit the shape-selectivity of acid zeotypes [93]: small-pore frameworks like H-SAPO34 [94] yield selectively light olefins (MTO), while medium and large pore materials, like H-ZSM5 [95,96], yield gasoline as the main product (MTG). Acid protons are introduced in zeotype frameworks as charge-compensation for low valence dopant ions. In principle, isomorphous substitution of a framework cation with any low valence dopant can be employed: M^{3+}/Si^{4+} replacements in zeolites; M^{2+}/Al^{3+} and M^{4+}/P^{5+} substitutions in AlPOs, each need a charge compensation which can be accomplished by means of acid protons. Defining a scale of relative acidity for the possible dopants, and correlating the acidity with the chemical composition, would be very useful in optimizing the activity and/or selectivity of the catalysts without extensive testing of each dopant type. Comparative experimental studies have explored possible correlations of the catalytic activity for isostructural frameworks with the dopant type. Correlations have been proposed between the acid strength and the ionic radius [97] and with the electronegativity [98] of the dopant, and with the T–O_H–T' angle of the protonated oxygen with its nearest neighbor ions T and T' in the framework [99,100]. Comparing the properties for all possible dopant ions, however, is a challenging experimental task, owing to the influence of ill-controlled quantities in the catalyst after preparation and activation: isomorphous substitutions of low valence ions are often energetically unstable and difficult to achieve; and the use of stoichiometric amounts of different dopant ions during the synthesis may result in different concentrations of dopants in framework and extra-framework positions in the final product. Moreover, other active defect centers may be created in the catalyst, and the interaction between defect centers in the same region of the catalyst may alter their activity. Comparative experimental studies, therefore, are always limited to only a subset of the possible low valence ions allowed by the framework stoichiometry. The application of computer modeling techniques is very powerful in such a case: all the above variables can be easily controlled in a modeling study of the solid. Although calculations consider an idealized description of the acid catalyst, they enable us to compare the properties of different isomorphous dopants in the same framework type, excluding the influence of all the other factors that may affect experimental studies. Modeling represents therefore an ideal tool to define a relative scale of acidity for different dopant ions, and to grade their catalytic activity. In our periodic QM calculations described in Section 4, we have studied a set of 17 low valence dopant ions, isomorphously substituted in zeotypic frameworks; these are B^{3+}, Al^{3+}, Ga^{3+}, Co^{3+}, Mn^{3+} and Fe^{3+}/Si^{4+} in chabasite; Be^{2+}, Mg^{2+}, Ca^{2+}, Sr^{2+}, Cr^{2+}, Mn^{2+}, Fe^{2+}, Co^{2+}, Ni^{2+} and Zn^{2+}/Al^{3+}, and Si^{4+}/P^{5+} in AlPO-34. Not all the doped systems listed above have yet been obtained experimentally; for instance the Sr^{2+}/Al^{3+} and Mn^{3+}/Si^{4+} substitutions. We have, however, examined them computationally, with the aim of extending the range of dopants considered and of highlighting the possible trends in the calculated properties as a function of the chemical features of the dopant ions.

In our computational work, we chose to screen the relative acid strength of the low valence dopant ions by calculating their OH stretching frequency, ν_{OH}. Both acidity and ν_{OH} depend on the strength of the OH bond, and these two observables are often assumed to correlate [101]: a stronger OH bond results in a higher value of ν_{OH} and a weaker acidity of the site. Of course, ν_{OH} is also observable by IR measurements on the solid acid catalysts. In this respect, we know that the HF Hamiltonian employed in our calculations overestimates the calculated stretching frequencies, by $\sim$12% compared to experiment. This error is systematic—a feature that has given rise in the literature to the habit of scaling the calculated HF value of frequencies by a 'golden factor' of 0.89 [102]. We do not plan here to compare our calculated frequencies with experiment, but only to compare the calculated value of ν_{OH} for the different dopant ions, to grade their acidic strength. We shall not, therefore, scale the calculated values of ν_{OH}. The OH stretching frequencies have been obtained, for the equilibrium structure of each dopant investigated, by calculating numerically the dynamical matrix at the Γ point of reciprocal space. Diagonalization of the dynamical matrix yields the phonon spectrum of the system, in the harmonic approximation, from which we have derived the values of ν_{OH}.

Our systematic study enables us to investigate the possible correlations between the calculated frequencies (acidity) and, first, the atomic properties of the dopant M (ionic radius and electronegativity) or, secondly, the local geometrical and electronic structure of the active site in the framework (M–O, M–H and O–H bond distances, M–O_H–T bond angle, electric field gradient). Results are summarized in Table 10, and presented in

Table 10
Equilibrium structural parameters for the low valence ions examined in chabasite or AlPO-34, and calculated OH stretching frequencies

Dopant	$R(M–O_{1,3})$	$R(M–O_H)$	$R(M–H)$	$M–O_H–P$	r	EN	ν_{OH}
Trivalent dopant ions in chabasite							
Si^{4+}	1.612			145.7	0.42	1.90	
B^{3+}	1.369	2.485	2.803	141.9	0.23	2.04	4238
Al^{3+}	1.689	1.899	2.418	128.0	0.51	1.61	4141
Ga^{3+}	1.762	1.992	2.523	126.2	0.62	1.81	4157
Fe^{3+}	1.829	2.066	2.612	123.6	0.64	1.83	4195
Co^{3+}	1.797	2.049	2.579	125.8	0.63	1.88	4243
Divalent dopant ions in AlPO-34							
Al^{3+}	1.726			141.6	0.51	1.61	
Be^{2+}	1.546	2.309	2.548	141.2	0.35	1.57	4128
Mg^{2+}	1.876	2.084	2.421	132.4	0.66	1.31	4037
Ca^{2+}	2.204	2.408	2.986	126.0	0.99	1.00	4140
Sr^{2+}	2.411	2.555	3.203	116.2	1.12	0.95	4195
Cr^{2+}	2.024	2.356	2.871	127.5	0.89	1.66	4243
Mn^{2+}	2.027	2.265	2.806	127.8	0.80	1.55	4194
Fe^{2+}	1.982	2.191	2.733	129.0	0.74	1.83	4157
Co^{2+}	1.943	2.141	2.669	129.3	0.72	1.88	4192
Ni^{2+}	1.899	2.192	2.749	126.4	0.69	1.91	4201
Zn^{2+}	1.907	2.189	2.684	131.3	0.74	1.65	4207
Tetravalent Si dopant in AlPO-34							
P^{5+}	1.512			141.6	0.35	2.19	
Si^{4+}	1.575	1.761	2.307	128.0	0.42	1.90	4186

The symbol R refer to the calculated distances in Å, as indicated; $M–O_H–T$ is the angle between the protonated oxygen and its two nearest T sites, in degrees; r the ionic radius of the dopant ion, in Å; EN the electronegativity of the dopant [84]; ν_{OH} the calculated OH stretching frequency, in cm^{-1}, from our HF calculations. For comparison with experiment, ν_{OH} should be multiplied by 0.89.

Figs. 16–18, in which the calculated ν_{OH} is plotted as a function of the parameters listed above.

Before examining the trends, it is of interest to note that our calculations predict Mg-AlPO to have far stronger acid properties than any of the other dopants examined, both in AlPO-34 and in chabasite. The calculated value of ν_{OH} is in fact more than 100 cm^{-1} lower in MgAPO-34 than for any other dopant examined. This finding is supported by experimental evidence [103]: MgAPO catalysts have been shown to form coke very quickly on the inner walls of the catalyst during acid-activated transformations of organic reagents—a process that requires a catalyst with high acid strength.

In the following discussion we shall examine the dependence of the calculated ν_{OH} on the different parameters introduced earlier in the discussion and employed in Figs. 16–18, to highlight the important factors that define the Brønsted acidity of doped zeotypes. No appreciable correlation between ν_{OH} and the electronegativity of the dopant ion emerges from an examination of Fig. 16. This result is consistent with the molecular-ionic picture of M–O and T–O bonds in the solid that we discussed earlier: when the oxygen ions of the framework are located between two cations with different formal charges, they form a covalent bond with the neighbor with higher charge, and an ionic bond with the neighbor with lower charge. The protonated

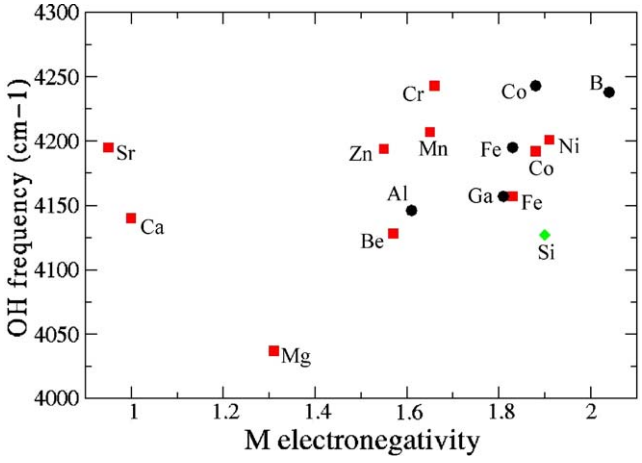

Fig. 16. Calculated OH stretching frequency, ν_{OH} (cm^{-1}), as a function of the electronegativity of the dopant ion [84]. Circles refer to dopant ions in chabasite; squares to 2+ ions in the Al framework position of AlPO-34, and the diamond to the Si/P replacement in AlPO-34.

oxygens responsible for the Brønsted acidity, are located between one of the host framework ions and the low valence dopant, with which they form a long and weak ionic bond (see Tables 5 and 10). In this environment, the behavior of the OH group is dominated by the bonding of the oxygen with the framework T ion, and is only marginally affected by the type of dopant. The

properties of the acid OH group, therefore, are not dictated by the electronic properties of the dopant ion, such as its electronegativity.

The low valence dopant, i.e. the $M^{n+}/T^{(n+1)+}$ substitutional center, corresponds to a defect with an effective negative charge of -1 in the solid. This defect creates a Coulomb potential in the neighboring region of the solid, centred on the dopant, and which decays as r^{-1}. The OH stretching vibration is altered by the change in the Coulomb forces; since frequencies are calculated by diagonalization of the dynamical matrix, which is the second derivative of the energy scaled by the atomic masses, the Coulomb contribution to ν_{OH} is the second derivative of the Coulomb potential, i.e. the electric field gradient (EFG) tensor, calculated in the equilibrium H position. The EFG created by a negative charge down shifts the frequency ν_{OH} and hence increases the proton acidity. The influence of the EFG on the OH stretching frequency is known from previous computational studies on a variety of systems, including the Al^{3+}/Si^{4+} defect center in zeolites [101,104,105]. There, the authors compared the properties of the same dopant ion (Al) in different zeolitic structures, and found a linear correlation between the calculated values of ν_{OH} and the EFG. In our work, we compare instead the calculated value of ν_{OH} for different dopant ions; in such a case, the correlation of ν_{OH} with the EFG (Fig. 17) is lost. Contrary to the study of Refs. [101,104,105], in which the local structure of the defect center (Al–O_H–Si) was very similar for each zeolitic structure examined, the local structural parameters of different dopant ions in the same polymorph show much more appreciable variations; for instance we see in Table 10 that the M–H distance varies from 2.321 Å (for Si^{4+}/P^{5+}) to 3.203 Å (for Sr^{2+}/Al^{3+}). It is not surprising, therefore, that the simple correlation found in Refs. [101,104,105] is lost here. Both the Coulomb potential and the EFG generated by the chemical substitution in the framework, decay on moving away from the dopant ion; we would therefore expect that the further away the acid proton is from the dopant in its equilibrium structure, the less the OH group is

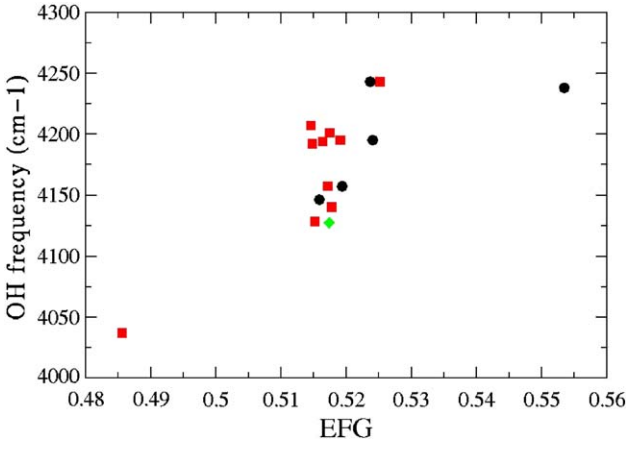

Fig. 17. Calculated OH stretching frequency, ν_{OH} (cm^{-1}), as a function of the electric field gradient in the equilibrium H position, in atomic units ($1\,au = 9.7174 \times 10^{21}\,V\,m^{-2}$). Symbols as in Fig. 16.

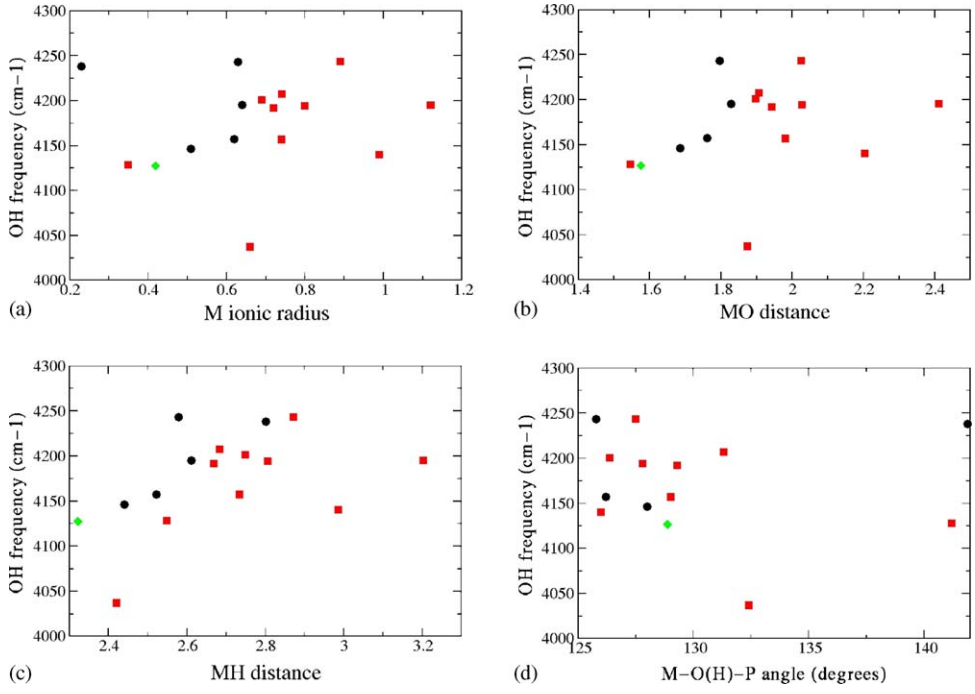

Fig. 18. Calculated OH stretching frequency, ν_{OH} (cm^{-1}), as a function of the structural parameters of the active site: (a) ionic radius of the dopant [84], in Å, (b) M–O distance, in Å, (c) M–H distance, in Å, and (d) M–O_H–P angle (°). Symbols as in Fig. 16.

perturbed by the M dopant. The correlation between ν_{OH} and the M–O and M–H equilibrium distances is therefore of interest to examine explicitly. Of course, the M–O distance is also a measure of the ionic radius of the dopant. Among all the structural parameters investigated, the MH distance (Fig. 18c) is perhaps the one that shows the best correlation with ν_{OH}. Zeolites and AlPOs, however, do not follow the same correlation, but rather form two distinct classes with a different shift in the calculated frequency. The dopant ions whose calculated ν_{OH} deviates most from a linear behavior as a function of the MH distance are Ca and Sr in AlPO. These are also the biggest dopant ions examined, and cause a large structural relaxation in the AlPO framework; the equilibrium structure of Ca and Sr in the AlPO framework is therefore substantially different from that of the other dopant ions. In particular the Brønsted OH group in Ca-AlPO34 and Sr-AlPO34 points towards a second oxygen of the framework. We consider that this hydrogen bonding-type of interaction contributes to downshifting the calculated value of ν_{OH} for the Ca and Sr dopants, and explains their deviation from the correlation of the acidic strength with the inverse of the MH distance. Be^{2+} in AlPO-34 and B^{3+} in chabasite also cause a different local structure around the Brønsted OH group, as they are stable in trigonal coordination. In the latter case, the framework is effectively broken along the bond between the dopant and the acid OH group, which contributes to increasing the M–H distance, and to decreasing the acid strength of the site, compared to the value expected on the basis of their ionic radius.

The results discussed above indicate that the biggest influence on the acid strength of doped zeolites and AlPOs is given by the ionic size of the dopant ion M. Within the structural limitations imposed by the relative size of dopant and host framework ions, smaller dopants yield shorter M–O and M–H distances in the equilibrium structure, and have lower ν_{OH}, hence are stronger acids. However, since the equilibrium local structure around the Brønsted OH group is very dissimilar among the dopant ions examined, correlating the acid properties with a single structural parameter related to the chemical nature of the dopant is not satisfactory. Subsets of dopants do exist, whose acid strength correlates with the chemical nature of the dopant; however, extension of the study to a wider range of low valence dopant ions shows that the correlation within the subsets is fortuitous, and not the result of a law with general validity. Our results do not therefore support a simple correlation between the acid strength of doped zeolites and AlPOs with either ionic radii [97], electronegativity [98] or bond angles [99,100] proposed in the literature. The complex behavior displayed by zeolites and AlPOs makes an optimization of their acid properties more suitable for a combinatorial approach, to which computational studies of the type reported here can make a substantial contribution.

5.2. Lewis acidity in transition metal-doped microporous AlPOs

The origin of Lewis acidity in microporous framework oxides has been extensively debated [106,107]. Experimental data considering the adsorption of Lewis basic molecules in doped AlPOs show the presence of two distinct adsorption sites, attributed to the framework Brønsted and Lewis acid sites [103,108]. When transition metal ions are incorporated in the framework, the Lewis acidity is likely to be associated with the transition metal centers. Not all the dopant ions, however, interact in the same way with Lewis bases; for instance, AlPOs containing Ni^{2+} ions have less pronounced Lewis acidity than their Co and Mn analogues [103]. The results of our QM calculations described in Section 4, in particular the calculated electronic distribution of the transition metal dopants and the orientation of the empty d atomic orbitals (AOs) on the metal site, can be used to examine the origin of their Lewis acidity. The dopants on which we focus here are the $2+$ and $3+$ transition metal ions in AlPO-34. In addition to the UHF calculations, the electronic structure of the Ni^{2+} dopant has been studied also with the B3LYP density functional Hamiltonian [36]. In transition metal-doped AlPOs, the unpopulated and/or partially filled d AOs of the transition metal site are obvious candidates to explain the presence or absence of Lewis acidity in the framework. To investigate this feature, we have calculated the total and spin electronic density of each metal dopant in its equilibrium structure [109]; the result is plotted in Fig. 19 for the low valent $2+$ ions, in the plane containing the M–O_H–P unit. In each plot, the continuous and dashed black and green lines are the isodensity levels calculated from the spin density. Not all the interstitial space within the microporous framework is accessible to adsorbed molecules: the Pauli repulsion caused by the overlap between the electronic density of the molecule and of the framework atoms, in fact, makes the adsorption process energetically unfavorable when the molecule is too close to the framework atoms. How close the adsorbed molecules can approach the framework and its active sites depends on the radial extent of the electronic density of the framework itself. To have an indication of this feature, we have calculated the total electronic density of the doped materials; in Fig. 19 we plot in red the isodensity level of 0.01 au, which represents an "effective" framework size.

The transition metal ions investigated have a partially filled d shell, with electronic configuration ranging between the $d^{(3)}$ of Cr^{3+}, to the $d^{(8)}$ of Ni^{2+}. All are stable in high spin state. The spin density of Fig. 19

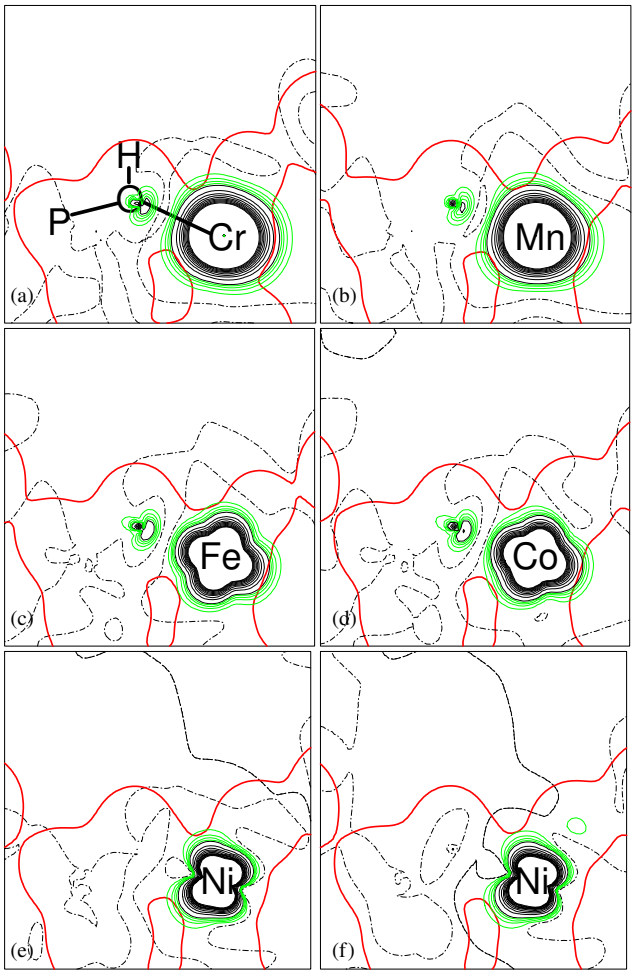

Fig. 19. Electron density maps for the undervalent 2+ transition metal ions in AlPO-34. The black and green lines represent the spin density, plotted between −0.05 and +0.05 au at linear steps of 0.005 au (black), and between 0.001 and 0.005 au at linear steps of 0.001 au (green). Continuous and dashed lines refer to positive and negative spin density, respectively. The continuous line is the isodensity level of 0.01 au calculated from the total electronic density, and represents the effective size of framework. The dopant ions are Cr^{2+} (a), Mn^{2+} (b), Fe^{2+} (c), Co^{2+} (d) and Ni^{2+} (e). The plot (f) refers to the solution for Ni^{2+}, calculated with the B3LYP Hamiltonian.

represents the distribution of the half-filled *d* AOs of the metal dopant. When considering the Lewis acidity of open shell transition metal ions in the high spin state, we have to distinguish between ions with less than half-filled *d* AOs (i.e. with electronic configuration $d^{(3)}-d^{(4)}$), and ions with *d* AOs at least half-filled (with electronic configuration $d^{(5)}-d^{(8)}$). In the former case the spin density represents the orbitals which are least active towards Lewis acidity: they are half-filled, while the other *d* orbitals are empty and therefore stronger Lewis acids. In the latter case, instead, the spin density represents the *d* orbitals responsible for the Lewis acidity: they are half-filled, while the remaining levels are completely occupied by two electrons, and hence inactive for Lewis acidity. We clearly see in Fig. 19 that the orientation and radial extent of the spin density differs according to the electronic configuration of the dopant ion. As a result, the extent of spin density that spills outside the Pauli repulsion area (thicker line) varies considerably among the dopants. The Lewis-active orbitals of Ni^{2+} are oriented along the framework; a molecule inside the microporous cages of a Ni-doped AlPO will therefore be subject to Pauli repulsion from the framework before having an effective interaction with the Lewis active orbitals of the Ni ion. This is not the case, instead, for Mn, Fe and Co dopant ions; molecules in Mn, Fe and Co-doped materials can undergo an appreciable chemical interaction with the Lewis-active orbitals before being repelled by the framework. We consider that this result explains effectively the origin of Lewis acidity in the latter frameworks, and its absence in the Ni-doped materials, in agreement with the experimental results of Ref. [103]. The presence of empty *d* states on the transition metal site, oriented perpendicularly to the framework structure, is necessary to initiate a Lewis acid/base interaction with adsorbed molecules.

To investigate whether this result depends on the Hamiltonian employed in the calculations, we repeated the study of Ni-AlPO34 with the B3LYP density functional. We find no significant qualitative changes, suggesting that our results have general validity. It is also important to notice, in Fig. 19, that for the 2+ dopant ions, spilling of the spin density outside the Pauli repulsion area is most effective on the side of the framework opposite to the proton. This feature suggests that the interaction of Lewis bases with the 2+ transition metal ions is most effective when the molecule can approach the framework from the side opposite to the protonated oxygen, while interaction of the adsorbed molecule with the Brønsted acid proton prevents an acid/base interaction of Lewis type with the transition metal ion. We refer to this structural requirement as an *attack from behind* of the Lewis basic molecule to the transition metal dopant [109]. This suggestion of our computational work is indirectly supported by experimental work on Co^{2+}-doped AlPOs [110,111], in which the authors found that to achieve complexation (Lewis interaction) of the framework Co^{2+} ions by acetonitrile, the Co–O_H bond must be broken, i.e. that Lewis and Brønsted acid interactions are mutually exclusive. Such a structural property of Lewis-type interactions is able to differentiate the Lewis acidity of different AlPO frameworks. We expect the transition metal ions to be more Lewis active when they are located in open regions of framework, where the space behind the dopant and the protonated oxygen is not protected by other framework ions. This is achieved in zeotypic frameworks with intersecting channels, or with single walls between large cages, such as the Chabasite topology. Dopants in framework structures with one-dimensional

channels made of 'double wall' building units, found in AlPO-5 and AlPO-11, are instead expected to be less Lewis active [109]. This result may explain why, experimentally, the Lewis acid behavior of Co-AlPO-5 towards the adsorption of acetonitrile was found similar to that of Co-AlPO-11 [81], but different from that of Co-AlPO-18 [110,111]. We leave open for further experimental verifications this prediction of the computational work.

5.3. Redox activity of transition metal ions in microporous AlPOs

Despite the importance of selective oxidation reactions in the manufacture of fine chemicals, finding a catalyst with the right compromise between redox activity and selectivity remains a challenging task [112]. Transition metal-doped AlPOs (MeAlPO) are active heterogeneous catalysts for the selective oxidation of hydrocarbons [2]; not all the transition metal ions, however, confer the same activity to the catalysts (see, e.g. [12,113,114]).

In Section 4.3 we have described the calculated energetics for the inclusion of $Cr^{II/III}$, $Mn^{II/III}$, $Fe^{II/III}$ and $Co^{II/III}$ ions in the framework of AlPO-34. Combining the information for the M^{II} and M^{III} dopants, we can evaluate the redox energy for the M^{II}/M^{III} couple in the MeAlPO catalysts, and calculate their redox potential. This has been performed by using hydrogen as reductant, according to Eq. (9):

$$M^{III}\text{AlPO-34} + \frac{1}{2}H_2 \xrightarrow{\Delta E^{III/II}} M^{II}\text{HAlPO-34}. \quad (9)$$

The results of our calculations are summarized in Table 11. Among the transition metal ions investigated, Fe is the most stable in 3+ oxidation state when incorporated in the AlPO framework, while Mn is the most stable as +2 ion. Cr and Co have intermediate behavior and can switch more easily between the two oxidation states. We have examined the redox behavior of the Co^{II}/Co^{III} couple in AlPO-34 also with a DFT-GGA Hamiltonian [115]. The calculated redox energy is consistent with the HF results: −1.18 eV/ion (GGA), and −1.07 eV/ion (HF).

The crystalline environment of the redox active ions plays a crucial role in determining their redox potential. In Table 11 we compare the redox energy of the M^{II}/M^{III} couples in AlPO-34, with the redox energy for the hexaaqua complexes $[M^{II}(H_2O)_6]$ and $[M^{III}(H_2O)_6]$, calculated with the same settings employed for the crystalline MeAlPOs. The redox energy for the same ion varies appreciably as a function of its chemical environment; this change is especially large for Cr, due to the destabilization of Cr^{3+} in a tetrahedral crystal field, which in Section 4.3 we estimated as being more than 1 eV. The interaction of the metal ions with their crystalline environment, therefore, is crucial in defining the redox potential. Tabulated redox potentials, such as the standard electrochemical series [84] (also reported in Table 11), do not apply to describe the redox behavior of different ions in the AlPO framework; the redox potential in the catalyst has to be evaluated explicitly, taking the effect of the crystalline matrix properly into account.

Table 11
Redox energies of the M^{II}/M^{III} couples investigated, as a function of the chemical environment of the redox-active ion M

$\Delta E^{II/III}$ (eV)	Cr	Mn	Fe	Co
AlPO-34, HF	−0.61	−2.67	+0.94	−1.07
AlPO-34, DFT [115]	—	—	—	−1.18
Hexaaqua complex	+0.34	−3.04	+0.65	−1.31
Standard cell voltage (V) [84]	−0.41	+1.54	+0.77	+1.92

The standard electrochemical cell voltage, V, is also reported (note that for the convention used in Eq. (9), and in the definition of the cell voltage, thermodynamically stable processes correspond to negative values of $\Delta E^{II/III}$ and positive of V).

The scale of redox strength proposed in Table 11, when coupled with experimental data on the catalytic activity of different dopant ions in the same AlPO framework, can help us identify the mechanistic details of the catalytic reaction.

As a general rule, each redox catalytic cycle in MeAlPOs will involve at least two elementary steps, which we can identify with the reduction of the M^{3+} dopant to Me^{2+}, and with its reoxidation from 2+ to 3+ oxidation state. The relative performance of the different M^{II}/M^{III} dopants will depend on which elementary step is rate determining for the catalytic reaction and in the experimental conditions examined. Framework type, temperature, partial pressures of reagents and products, can each influence the relative rate of the two elementary steps, and hence also the relative activity of Fe, Co, Mn and Cr-AlPO catalysts. If we assume that the rate determining step in the catalytic cycle involves the reduction of M^{3+} to M^{2+}, our calculations predict the relative activity to decrease in the order of MnAlPO > CoAlPO > CrAlPO > FeAlPO. An example has been reported by Thomas et al. [113]: MnAlPO and CoAlPO are found to have high activity in the regioselective oxidation of linear alkanes by molecular oxygen. The authors report that, in the course of the partial oxidation, the transition metal ions are reduced to their +2 states. If the rate determining step involves the reoxidation of the M^{2+} dopant ion to M^{3+}, we expect a reverse order of activity, i.e. FeAlPO > CrAlPO > CoAlPO > MnAlPO. Thomas et al. [12], for instance, reported that FeAlPOs shows catalytic activity superior to that of the Co and Mn-substituted analogues for the selective oxidation of cyclohexane in air. The authors attributed this results to the fact that only a

small proportion of the Co^{2+} and Mn^{2+} ions that are isomorphously incorporated into the AlPO-36, AlPO-11 and AlPO-5 structures are convertible into the +3 oxidation state by O_2 or dry air, in contrast to Fe^{2+} which is completely converted into Fe^{3+}. This behavior is in agreement with our results.

Finally, if the two elementary steps described above have comparable rate, we would expect CrAPO and CoAPO catalysts to be the most active, as Cr and Co are the ions that can more easily change their oxidation state in either direction. Experimental results by Luna et al. [114], concerning the redox activity of different dopants in the AlPO VPI-5 framework, for the oxidation of cyclohexane under mild conditions, show that CrAPO has the highest activity, and MnAPO the lowest. Comparing the relative activity of different dopants in the oxidation of cyclohexane from Refs. [12,114], suggests that the cyclohexane oxidation proceeds via different mechanisms in small and large pore AlPO catalysts. The VPI-5 structure has larger pore size than the catalysts used in Ref. [12]. In a small-pore material, the alkane molecule can only 'crawl' in the micropores of the catalysts, yielding an effective contact with the active sites; in contrast, the interaction is weaker in a large-pore material. We therefore expect kinetic control of the reaction in small-pore catalysts, and thermodynamic control in large-pore materials, explaining the different relative activity of the same dopant ions in different microporous architectures.

6. Modeling of reaction mechanisms

Until now, we have examined the chemistry of transition-metal dopant ions in the microporous framework of zeolites and AlPOs, and discussed the implications that it can have on the catalytic activity of the solid. Of course, ultimate computational control of the reaction steps taking place in the microporous environment should be seeked by modeling the complete reaction path, from the initial reagents to the final products, including the catalyst regeneration at the end of the catalytic cycle. This is still a formidable computational task; in principle, it requires us to identify all the stationary points (reagents, intermediates, products and transition states) of the potential energy surface, in the configurational space defined by the atomic coordinates of each constituent atom of the system (reagents, catalyst and solvent). Chemical intuition, mathematical algorithms, and calculated energy relative to the reagents help us limiting the possible options; however, locating all possible transition states and intermediates to define the reaction path is not straightforward. The study of reaction mechanisms in the porous systems is exemplified here by the epoxidation of alkenes on porous titanosilicates. Ti-doped silicates, in both their micro- and meso-porous variants, have remarkable catalytic efficiency in the oxidation of small-chain hydrocarbons, such as the conversion of alkenes to epoxides, under mild conditions and using peroxides as sacrificial oxidants [116,117]. Joint experimental and computational work in our Laboratory has recently been dedicated to study both the active site structures and the mechanisms of the catalytic reaction. For a detailed discussion of the computational work performed, and its relation to the computational and experimental literature, the reader is remanded to Ref. [43].

XAS, IR and UV-vis spectroscopies, and computational studies have demonstrated that the Ti^{IV} center is four-coordinate in a dehydrated medium, and reversibly increases its coordination number to 5 or 6 under exposure to water or peroxides [118,119]. The mechanism of the catalytic reaction is thought to include as intermediate a Ti-peroxo complex; the exact nature of the oxygen-donating species in the catalytic cycle, however, is still under debate. In microporous titanosilicates, cleavage of one or more Ti–O–Si bonds of the Ti with the crystalline matrix is known to occur, generating tripodal $(–SiO–)_3Ti(–OH)$ and/or bipodal $(–SiO–)_2Ti(–OH)_2$ sites [120]; the presence of the terminal OH groups is shown by FTIR. In mesoporous Ti-MCM41, a combination of in situ FTIR and XAS data identified unambiguously the presence of tripodally anchored Ti^{IV} centers [121,122]. A tripodal Ti^{IV} species is therefore a valid starting model of the active site, which is applicable to both micro- and meso-porous titanosilicates. We have modeled this site in our calculations with the $(H_3SiO–)_3Ti–OH$ molecular fragment shown in Fig. 20, as described in Section 2.3. Concerning the reaction mechanism, several pieces of information are available in the literature (see [43] and references therein). Ti-peroxo intermediates in the liquid phase are known to contain both η^1 and η^2 species, in which the peroxide molecule acts as a mono-(η^1) or bi-dentate (η^2) ligand. Neutral, anionic and radical Ti-peroxo species have all been identified in protic solvents. Each combination of coordination mode and electronic states listed above has been suggested to apply in

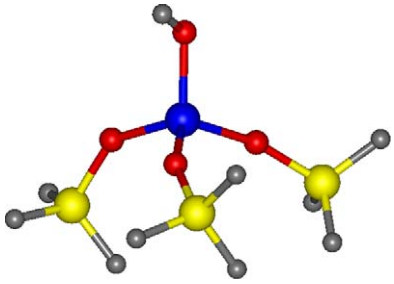

Fig. 20. $(H_3SiO–)_3Ti–OH$ molecular fragment employed in our calculations to represent a tripodally anchored Ti^{IV} species in titanosilicate catalysts.

titanosilicate heterogeneous catalysts. An accurate structural and energetic characterization of these combinations, which can be achieved with a combination of modeling and in situ experimental studies under operating conditions, would provide valuable information on the true reaction mechanism.

In the first step of our investigation, we have therefore employed DFT calculations, using the $(H_3SiO–)_3Ti–OH$ cluster, to study the geometries and energies of the possible Ti-peroxo complexes suggested as oxygen-donating intermediates in the catalytic cycle. H_2O_2 has been used as oxidant, for computational convenience, although selected calculations (not reported here) have been repeated with TBHP [43] to compare with experimental results. We have initially optimized the geometries of hydrated (six-coordinated) and de-hydrated (five-coordinated) η^2 complexes, arising from the reaction of H_2O_2 (and water) with the $(H_3SiO–)_3Ti–OH$ cluster. Formation of the Ti(η^2–OOH) complex occurs via attack of the peroxide on the tetrahedral Ti center, with subsequent proton transfer from the peroxide to the hydroxyl ligand. The anionic and radical η^2 species are found $\sim$600 and $\sim$400 kJ/mol unstable, suggesting that they are not accessible under mild reaction conditions. In agreement with the widely accepted proposal that tetrahedral Ti can reversibly expand its coordination to six in hydrated media, we find that all the η^2 Ti-peroxo complexes are stably hydrated. The water ligand is weakly bound to Ti (with a hydration energy of 25–46 kJ/mol depending on the charge state of the peroxo ligand), suggestive of physisorption, and does not influence significantly the mode of coordination of the peroxo ligand to Ti. The η^2 Ti-peroxo intermediate is 19 kJ/mol more stable than the isolated Ti center and H_2O_2 molecule when dehydrated, and 44 kJ/mol when hydrated. A similar series of results is observed for the η^1 intermediate, which arises from a monodentate attack of the peroxide molecule to Ti, and subsequent proton transfer from the peroxide to the OH ligand. The formation of an anionic η^1 peroxo intermediate is unfavorable, with a cost of $\sim$600 kJ/mol. In accordance with the results for the η^2 species, hydration is exothermic (by 24 kJ/mol) also for the η^1 Ti-peroxo adduct, and the η^1 intermediate is stable with respect to the isolated H_2O_2 and Ti center; the energy gain is of 41 kJ/mol when dehydrated, and 65 kJ/mol when hydrated. We further examined the effect of proton transfer on the structure and energetics of the two Ti-peroxo intermediates. This has been achieved by transferring the peroxidic proton between the two peroxidic oxygens, and reoptimizing the structures. In the η^2 complex, the original structure has been restored, while for the η^1 adduct this procedure produced a new, stable η^1 Ti-peroxo complex, denoted as Ti(η^1–O_2H_2). This is formed through a monodentate (η^1) binding of H_2O_2 to Ti, with hydrogen bonding (but not deprotonation) from the peroxide molecule to the OH ligand. Upon hydration of this cluster, the water ligand interacts with the peroxide molecule and not directly with the Ti center. The Ti(η^1–O_2H_2) adduct is the most stable, with a formation energy of −42 and −87 kJ/mol in dehydrated and hydrated states, respectively. The three stable intermediates described above are illustrated in Fig. 21.

In addition to the DFT calculations, we have performed in situ structural studies of Ti-MCM41 using EXAFS. During the actual epoxidation, the XAS study yields the steady-state structure at the Ti^{IV} center, from which we derived that six oxygens surround the Ti, two of them at distances greater than 2.2 Å. XAS measurement also indicate that, at steady-state, no alkene is bound to the Ti^{IV}-centred active site.

Each of the calculated structures for the η^1 and η^2 intermediates has been used to generate simulated EXAFS data (using full multiple scattering procedures), and compared to the experimental result. The six-coordinate η^1 and η^2 intermediates have an equally good fit (the result for the η^2 complex is shown in Fig. 22), while none of the other electronic states examined, which have higher calculated energy, agrees with the

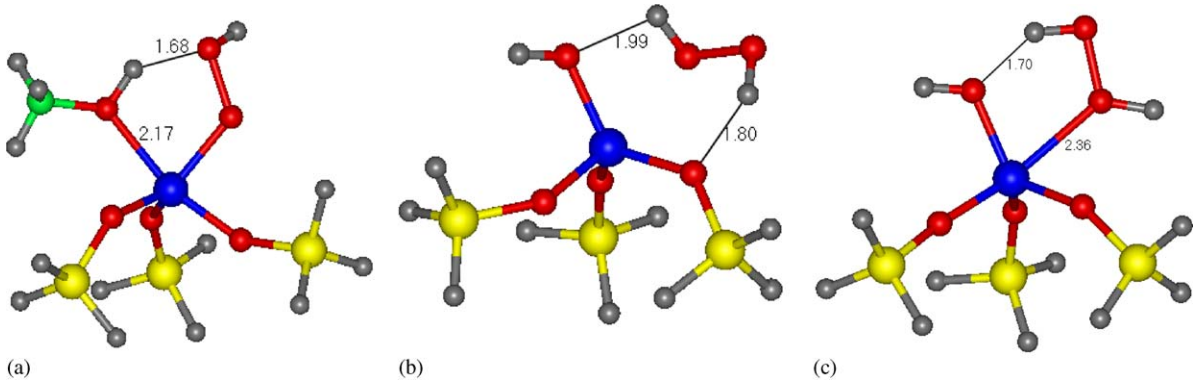

Fig. 21. Geometry optimized structure of the three stable Ti-peroxo intermediates found in our calculations: (a) η^1 monodentate complex; (b) η^2 bidentate complex; and (c) η^1 O_2H_2 complex.

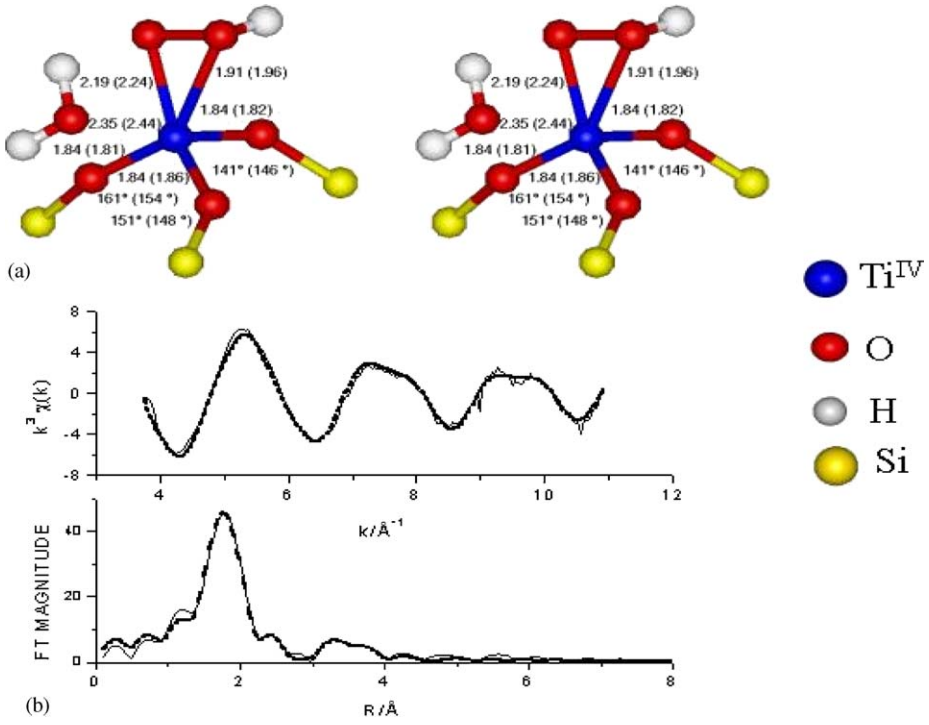

Fig. 22. (a) Structure of the η^2 Ti-peroxo intermediate as determined from Ti K-edge EXAFS data and DFT calculations (DFT numbers are in parantheses); (b) correspondence between experimentally determined EXAFS (full line) and computed data (dashed line) for the Ti^{IV}-centred catalyst during epoxidation.

experimental observations. For the Ti(η^1–O_2H_2) the agreement with experiment is not good, even though its calculated formation energy is the most favorable. Because the peroxide molecule remains intact upon binding to the Ti site, it is possible that this intermediate could have a short lifetime under reaction conditions, and be undetectable by XAS.

Once the stable intermediates have been identified, we proceeded with the characterization of the transition states (TS) that lead to their formation. This procedure enables us to estimate the activation barrier for the formation of each structure, and hence judge whether such intermediates can be reached under different reaction conditions. The TS in a simulated reaction path is defined as a saddle point in the potential energy surface (PES), which corresponds to a Hessian matrix (second derivatives of the energy with respect to the nuclear coordinates) with one negative eigenvalue. The search for a TS in the presence of structural constraints is made more difficult by the fact that the constraints themselves give rise to negative eigenvalues in the Hessian matrix. We recall that in our work we have fixed the outermost Si ions of the cluster during the geometry optimizations, and also in the TS search, to represent the rigidity imposed on the active site by the crystalline matrix. However, the effect of these constraints should be minor, compared to the mode associated with the TS. The TS search in these conditions corresponds to searching for a point in the PES in which the Hessian matrix has one *dominant* negative eigenvalue; this has been performed in our calculations by linear and quadratic synchronous transit techniques, coupled by mode-following algorithms [123,124]. From the TS, the intrinsic reaction coordinate is defined as the eigenvector of the Hessian associated with the dominant negative eigenvalue; this vibrational mode tracks, on either side of the TS, the steepest descent path to reagents and products. Thus, once the TS for a reaction step is known, the reagent and product associated with it can be unequivocally identified. For the η^2 intermediate, for instance, the dominant negative eigenvalue is associated with a H-stretching mode from the peroxide fragment to the Ti–OH group. Once the vibrational mode indicative of the reaction pathway is found, this information has been used to form new starting geometries, and to determine the associated reactant and product. We moved the H atom manually on either sides of the TS, and used these starting configurations in geometry optimizations to track the full reaction path. Fig. 23 shows the resulting energy profile for η^1 and η^2 intermediates; the calculated activation barriers are in each case of $\sim$40 kJ/mol. Both are therefore expected to be present during the catalytic turnover.

Alkene epoxidation is expected to occur on one of the Ti-peroxo intermediates described above. Again, the particular mechanism in this reaction step is unknown. The first question to understand is which oxygen in each

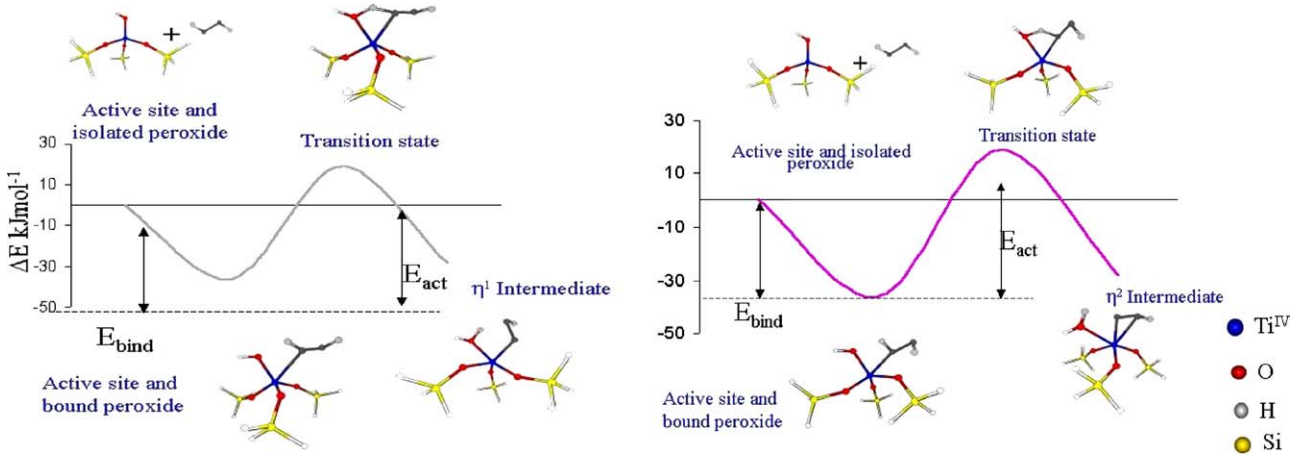

Fig. 23. Calculated energetic pathways, from the bare active site and isolated peroxide to the η^1 (left) and η^2 intermediates (right).

of the peroxo complexes is most likely to be donated to the alkene. Since the interaction of an electron-rich alkene double bond with a nucleophilic peroxidic oxygen atom is repulsive, it is thought that the most electrophilic oxygen will form the epoxide. A Mulliken population analysis of the oxygens in the energy-minimized intermediates shows that, in each structure, the peroxide oxygen closest to the Ti center has lower net charge. The only exceptions are due to the presence of electron-withdrawing groups as substituents in the structure [125]. This result suggests that the alkene will preferentially interact with the oxygen atom closest to Ti in the intermediate. In order to define suitable starting geometries for modeling the interaction of alkenes with the Ti-peroxo intermediates, we followed a frontier orbital approach, and compared the energies of the HOMO and LUMO in the intermediate and alkene molecule. For both η^1 and η^2 structures, the interaction between the LUMO of the catalyst and the HOMO of the alkene is favorable (the energy gap is 200 kJ/mol smaller) compared to the converse interaction involving the LUMO on the alkene and the HOMO of the catalyst. Furthermore, the LUMO-HOMO gap for propene is $\sim$50 kJ/mol lower than for ethene, suggesting a higher reactivity of propene, also known from experiment. The starting geometries for modeling the interaction of the alkene with the Ti-peroxo intermediates have therefore been constructed by orienting the alkene molecule so that its HOMO overlaps with the LUMO of the catalyst. We start our discussion from the η^1 complex, shown in Fig. 24. Energy optimization of this structure results in spontaneous formation of the epoxide, expulsion of water and regeneration of the original catalyst. This reaction step is illustrated in Fig. 25a; at no point does the alkene interfere with the anchoring silanol bonds. Initial docking of the alkene molecule to the Ti-peroxo intermediate incurs a small energetic cost, of less than

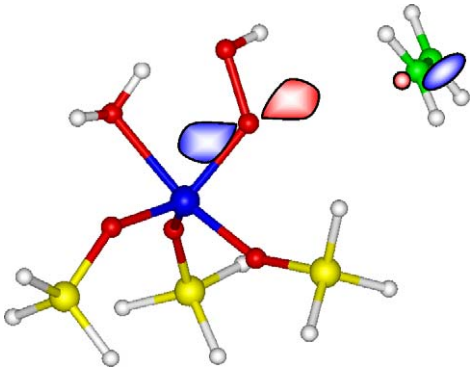

Fig. 24. Starting geometry for the ethene attack on the peroxidic oxygen closest to the Ti center, in a η^1 Ti-peroxo complex.

15 kJ/mol; however, formation of the epoxide is highly exothermic. The products are 171 kJ/mol more stable than the isolated reactants.

Interaction of the alkene with the η^2 intermediate was initiated by positioning the alkene double bond parallel to the peroxide molecule; optimization of this structure leads to an alcohol-type functionality (see Fig. 25b), which may be responsible for the formation of diol by-products observed experimentally [126,127]. The OH ligand hinders other directions of attack of the alkene molecule to the peroxidic oxygen closest to Ti. We finally considered the Ti(η^1–O_2H_2) intermediate; as for the other η^1 intermediate, energy minimization results in spontaneous epoxide formation, as shown in Fig. 25c.

Our calculations, therefore, are able to elucidate the complete reaction mechanism (see Fig. 26) by which the titanosilicate catalyst operates in the epoxidation of alkenes under mild conditions and using peroxide molecules as oxidant. This detailed information is crucial to optimize and/or modify the catalytic performance; although applied now to a reaction that is well known to experimental studies, similar reaction

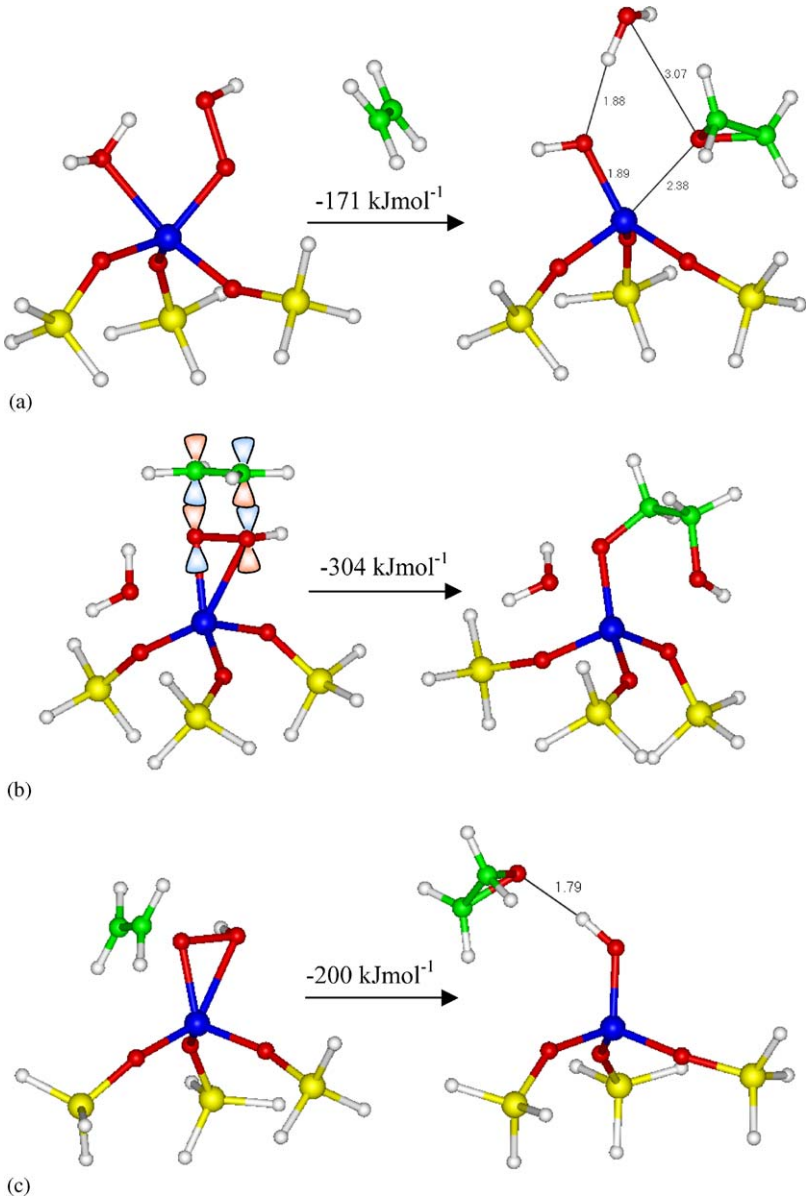

Fig. 25. Calculated initial and final states for the interaction of ethene with (a) the η^1, (b) the η^2, and (c) the η^1–O_2H_2 Ti-peroxo intermediates, and calculated reaction energies.

modeling strategies will be increasingly applied in the future to *design* computationally *new* catalysts and reactions pathways, to input into experimental programmes.

7. Conclusions

We have presented a thorough computational study of pure and transition metal-doped zeolite and AlPO frameworks, in which we have examined several fundamental topics of these heterogeneous catalysts. Periodic QM calculations show that AlPO frameworks have a molecular-ionic character, and are composed of discrete Al^{3+} and PO_4^{3-} ions, while zeolites are built from a continuous semicovalent network of Si–O bonds. Analysis of the calculated electronic density also suggests that the T–O (T = Al, Si, P) bonding features are a *local* property of the solid, and are only marginally affected by the long-range crystalline structure. A statistical analysis of the structure of known zeolite and AlPO polymorphs shows that in both framework types the local geometry of the T sites can easily adapt to the three-dimensional connectivity of the structure, or to substitutent atoms, by bending the flexible T–O–T angles. This feature is crucial to enable the rich polymorphic variety and defect chemistry observed in zeolites and AlPOs, and also plays a role in defining

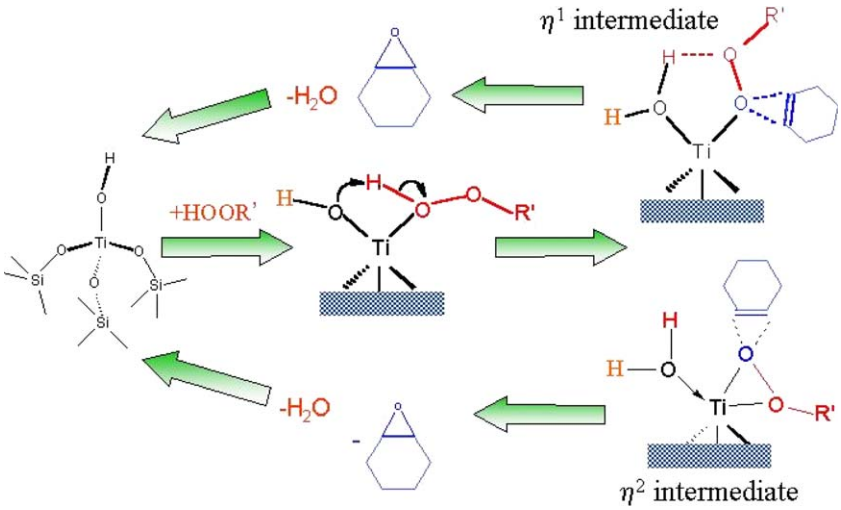

Fig. 26. This schematic picture shows how, by elimination of the epoxide and the alcohol (R'OH from the η^1 or η^2 intermediate), the Ti active center is generated.

their catalytic activity. The flexible nature of the framework, in fact, enables the coordination number of the active site in the framework to vary during the catalytic cycle without a high energetic toll. In agreement with the ionicity of the Al–O bonds, Al^{3+} introduces little angular strain in the AlO_4 tetrahedra, compared with the covalent PO_4^{3-} unit, where angular constraints are more important.

The chemistry of the undoped frameworks influences the incorporation of different dopant ions: ionic substitutional dopants replace more readily Al in AlPOs than Si in zeolites. We have examined 23 substitutional dopants in the isostructural framework of chabasite and AlPO-34 and with a consistent computational technique, enabling extensive comparisons between the atomic, chemical and structural properties of the dopant, and their effect on the microporous framework. The dopant ions examined cover most of the isomorphous framework replacements known to occur experimentally, but also framework replacements that have not yet been achieved. In this case, ab initio modeling techniques are employed in a predictive way. Our results show that the ionic size of the dopant has a major role in characterizing the properties of the doped frameworks; it has a clear influence on a range of features of the doped materials, from the local distortion around the dopant to the incorporation energy of the dopant in the framework, its site ordering, and the acidity of the catalyst. Our calculations, however, do not suggest simple correlations between the atomic properties of the dopant ion and the catalytic activity of the doped frameworks. The complex catalytic behavior displayed by zeolites and AlPOs depends on a combination of structural and chemical properties of the active site, which must be evaluated on a case-by-case basis. Accurate QM calculations can help us to characterize this complex behavior. In order to rationalize the defect chemistry of zeotypes, we have partitioned the framework T sites into *caged* and *free* according to their local structural constraints. In the former case, the framework forms a rigid structure around the site, while the free T sites are located in more flexible regions of the framework. Dopant ions are preferentially located in the free T sites, a feature that is also essential to enable their chemical reactivity.

From a methodological point of view, the extended nature of crystalline zeolites and AlPOs is best suited for techniques that employ periodic boundary conditions; however, the local nature of the chemistry in the framework of zeolites and AlPOs is such that small molecular fragments cut out of the three-dimensional solid are representative enough to include the major contributions to the chemical reactivity of the active sites. Furthermore, the framework flexibility absorbs chemical and structural strains, and minimizes the effect of long-ranged structural constraints on the active sites. Less expensive molecular calculations can therefore be employed to study the mechanisms of reactions catalyzed by zeolites and AlPOs. This feature has been exploited to perform a computational study of the alkene epoxidation on titanosilicates. We have identified a range of intermediates and transition states in the potential energy surface that links reagents and products. Both mono- (η^1) and bi-dentate (η^2) attack of H_2O_2 to the Ti site can occur, yielding three stable intermediates. Upon interaction of the intermediates with alkenes, the η^1 species lead to epoxidation, while the η^2 species is potentially responsible for the formation of diol byproducts. Mastering the atomic steps of a catalytic cycle is crucial in the design of new catalysts with improved activity and/or selectivity, which is a field that will greatly benefit from the powerful insight enabled by modeling techniques.

Acknowledgments

We thank EPSRC for their support of this work, in particular for an Advanced Research Fellowship awarded to FC, and the Royal Society for a grant to FC to purchase computer equipment. We also thank the authors of CRYSTAL for providing a pre-released version of the code.

References

[1] H. van Bekkum, E.M. Flanigen, P.A. Jacobs, J.C. Jansen, Introduction to Zeolite Science and Practice, Elsevier, Amsterdam, 2001.
[2] J.M. Thomas, Angew. Chem. Int. Ed. 38 (1999) 3588.
[3] J.M. Thomas, Angew. Chem. Int. Ed. 27 (1988) 1673.
[4] D.W. Lewis, C.R.A. Catlow, J.M. Thomas, Chem. Mater. 8 (1996) 1112.
[5] D.W. Lewis, D.J. Willock, C.R.A. Catlow, J.M. Thomas, G.J. Hutchings, Nature 382 (1996) 604.
[6] S.A. Schunk, L. Schüth, in: Molecular Sieve Science and Technology, Vol. I, Spinger, Berlin, 1998, p. 229.
[7] R. Fricke, H. Kosslick, G. Lischke, M. Richter, Chem. Rev. 100 (2000) 2303.
[8] Y. Ma, W. Tong, H. Zhou, S.L. Suib, Micropor. Mesopor. Mater. 37 (2000) 243.
[9] J.M. Thomas, Sci. Am. 286 (1992) 82.
[10] A. Corma, Curr. Opin. Solid State Mater. Sci. 2 (1997) 63.
[11] G. Perego, G. Bellussi, C. Corno, M. Taramasso, F. Buonomo, A. Esposito, Stud. Surf. Sci. Catal. 28 (1986) 129.
[12] J.M. Thomas, R. Raja, G. Sankar, R.G. Bell, Acc. Chem. Res. 34 (2001) 191.
[13] M. Hartmann, L. Kevan, Chem. Rev. 99 (1999) 635.
[14] J.M. Thomas, C.R.A. Catlow, G. Sankar, Chem. Commun. (2002) 2921.
[15] W.J. Mortier, Compilation of Extra-framework Sites in Zeolites, Butterworth-Heinemann, London, 1982.
[16] D.H. Olsen, Zeolites 15 (1995) 439.
[17] G. Sankar, J.M. Thomas, Top. Catal. 8 (1999) 1.
[18] C. Zenonos, G. Sankar, F. Corà, D.W. Lewis, Q.A. Pankhurst, C.R.A. Catlow, J.M. Thomas, Phys. Chem. Chem. Phys. 4 (2002) 5421.
[19] P.A. Barrett, G. Sankar, C.R.A. Catlow, J.M. Thomas, J. Phys. Chem. 100 (1996) 8977.
[20] F. Corà, G. Sankar, C.R.A. Catlow, J.M. Thomas, Chem Commun. 2002, 734.
[21] C.R.A. Catlow, Computer Modelling in Inorganic Crystallography, Academic Press, London, 1997.
[22] M. Sierka, J. Sauer, Faraday Discuss. 106 (1997) 41; J. Sauer, K.-P. Schroder, V. Termath, Collect. Czech. Chem. Commun. 63 (1998) 1394.
[23] R.A. van Santen, Catal. Today 38 (1997) 377; R.A. van Santen, J. Mol. Catal. A 3 (1997) 405.
[24] P. Sherwoord, A.H. de Vries, S.J. Collins, S.P. Greatbanks, N.A. Burton, M.A. Vincent, I.H. Hillier, Faraday Discuss. 106 (1997) 79. [25] J.M. Sanders, M. Leslie, C.R.A. Catlow, J. Chem. Soc. Chem. Commun. 19 (1984) 1271.
[26] J.D. Gale, N.J. Henson, J. Chem. Soc. Faraday Trans. 90 (1994) 3175.
[27] J.D. Gale, J. Chem. Soc. Faraday Trans. 93 (1997) 629.
[28] C. Pisani, R. Dovesi, C. Roetti, Hartree-Fock Ab Initio Treatment of Crystalline Systems, Lecture Notes in Chemistry, Vol. 48, Springer, Heidelberg, 1988.
[29] V.R. Saunders, R. Dovesi, C. Roetti, M. Causà, N.M. Harrison, R. Orlando, C.M. Zicovich-Wilson, K. Doll, B. Civalleri, CRYSTAL2002 User's Manual, University of Torino, Torino, 2002.
[30] www.crystal.unito.it/Basis_Sets/ptable.html
[31] I. Saadoune, F. Corà, C.R.A. Catlow, J. Phys. Chem. B 107 (2003) 3003.
[32] K. Doll, V.R. Saunders, N.M. Harrison, J. Quantum Chem. 82 (2001) 1.
[33] B. Civalleri, Ph. D'Arco, R. Orlando, V.R. Saunders, R. Dovesi, Chem. Phys. Lett. 348 (2001) 131.
[34] S.H. Vosko, L. Kilk, M. Nusair, Can. J. Phys. 58 (1980) 1200.
[35] J.P. Perdew, Y. Wang, Phys. Rev. B 45 (1992) 13244.
[36] A.D. Becke, J. Chem. Phys. 98 (1993) 5648.
[37] R. Dovesi, F. Freyria Fava, C. Roetti, V.R. Saunders, Faraday Discuss. 106 (1997) 173.
[38] G.N. Vayssilov, R.A. van Santen, J. Catal. 175 (1998) 170.
[39] A. Becke, Phys. Rev. A 38 (1988) 3098.
[40] J. Perdew, Y. Wang, Phys. Rev. B 33 (1986) 8800.
[41] Dgauss$^{4.1}$, Oxford Molecular Inc.
[42] DMOL$^{4.2}$, Molecular Simulations Inc.
[43] C.M. Barker, D. Gleeson, N. Kaltsoyannis, C.R.A. Catlow, G. Sankar, J.M. Thomas, Phys. Chem. Chem. Phys. 4 (2002) 1228.
[44] H.N. Ng, C. Calvo, Can. J. Phys. 54 (1976) 638.
[45] N. Thong, D. Schwarzenbach, Acta Crystallogr. A 35 (1979) 658.
[46] B. Civalleri, C.M. Zicovich-Wilson, P. Ugliengo, V.R. Saunders, R. Dovesi, Chem. Phys. Lett. 292 (1998) 384.
[47] R.F. Bader, in: Atoms in Molecules: A Quantum Theory, International Series of Monographs on Chemistry, Vol. 22, Clarendon Press, Oxford, 1990.
[48] A. Tuel, S. Caldarelli, A. Meden, L.B. McCusker, C. Baerlocher, A. Ristic, N. Rajic, G. Mali, V. Kaucic, J. Phys. Chem. B 104 (2000) 5697.
[49] N. Hu, A. Navrotsky, C.-Y. Chen, M.E. Davies, Chem. Mater. 7 (1995) 1816.
[50] P. Richet, Y. Bottinga, L. Denielou, J.P. Petitet, C. Tequi, Geochim. Cosmochim. Acta 46 (1982) 2639.
[51] I. Petrovic, A. Navrotsky, M.E. Davis, S.I. Zones, Chem. Mater. 5 (1993) 1805.
[52] P.M. Piccione, C. Laberty, S. Yang, M.A. Camblor, A. Navrotsky, M.E. Davis, J. Phys. Chem. B 104 (2000) 10001.
[53] A. Navrotsky, I. Petrovic, Y. Hu, C.-Y. Chen, M.E. Davis, Micropor. Mater. 4 (1995) 95.
[54] F. Corà, C.R.A. Catlow, J. Phys. Chem. B 105 (2001) 10278.
[55] F. Corà, C.R.A. Catlow, D.W. Lewis, J. Mol. Catal. A: Chem. 166 (2001) 123.
[56] C.H. Baerlocher, W.M. Meier, D.H. Olsen, Atlas of Zeolite Framework Types, 5th Edition, Elsevier, Amsterdam, 2001.
[57] M.M.J. Treacy, K.H. Randall, S. Rao, J.A. Perry, D.J. Chadi, Z. f. Kristall. 212 (1997) 768.
[58] J. Klinowski, Curr. Opin. Solid State Mater. 3 (1998) 79.
[59] O. Delgado Friedrichs, A.W.M. Dress, D.H. Huson, J. Klinowski, A.L. Mackay, Nature 400 (1999) 644.
[60] M.D. Foster, R.G. Bell, J. Klinowski, to be published.
[61] M.D. Foster, R.G. Bell, J. Klinowski, Stud. Surf. Sci. Catal. 135 (2001) 16P13.
[62] Z. Fu, D. Yin, Q. Li, L. Zhang, Y. Zhang, Micropor. Mesopor. Mater. 29 (1999) 351.
[63] C. Prieto, T. Blasco, M. Camblor, J. Perez-Pariente, J. Mater. Chem. 10 (2000) 1383.
[64] K. Chao, A.C. Wei, J. Electron Spectrosc. Relat. Phenom. 119 (2001) 175.
[65] M.-J. Diaz-Cabañas, P.A. Barrett, M.A. Camblor, Chem. Commun. (1998) 1881.
[66] G.-Y. Yang, S.C. Sevov, Inorg. Chem. 40 (2001) 2214.

[67] A. Goiffon, G. Bayle, R. Astier, J.C. Jumas, M. Maurin, E. Philippot, Rev. Chem. Miner. 20 (1983) 338.
[68] P.A. Barrett, G. Sankar, C.R.A. Catlow, J.M. Thomas, J. Phys. Chem. 100 (1996) 8977.
[69] G. Sankar, D. Gleeson, J.M. Thomas, A.D. Smith, J. Synchrotron Radiat. 8 (2001) 625.
[70] G. Sankar, J.M. Thomas, C.R.A. Catlow, Top. Catal. 10 (2000) 255.
[71] Y. Xu, J.W. Couves, R.H. Jones, C.R.A. Catlow, G.N. Greaves, J. Chen, J.M. Thomas, J. Phys. Chem. Solids 10 (1991) 1229.
[72] N.N. Tusar, A. Tuel, I. Arcone, V. Kaucic, Prog. Zeolites Micropor. Mater. 105 (1997) 501.
[73] A. Ristić, N.N. Tušar, I. Arĉon, T. Thibault-Starzyk, D. Hanžel, J. Czyzniewska, V. Kauĉiĉ, Micropor. Mesopor. Mater. 56 (2002) 303.
[74] J. Sauer, Chem. Rev. 89 (1989) 199;
J. Sauer, in: C.R.A. Catlow (Ed.), Modelling of Structure and Reactivity in Zeolites, Academic Press, London, 1992, p. 183.
[75] M. Brändle, J. Sauer, J. Am. Chem. Soc. 120 (1998) 1556.
[76] M. Sierka, J. Sauer, Faraday Discuss. 106 (1997) 41.
[77] F. Haase, J. Sauer, J. Am. Chem. Soc. 117 (1995) 3780.
[78] P. Ugliengo, B. Civalleri, C.M. Zicovich-Wilson, R. Dovesi, Chem. Phys. Lett. 318 (2000) 247.
[79] R.A. Jackson, C.R.A. Catlow, Mol. Simul. 1 (1988) 207.
[80] D. Müller, E. Jahn, G. Ladwig, U. Haubenreisser, Chem. Phys. Lett. 109 (1984) 332.
[81] J. Jänchen, M.P.J. Peeters, J.H.M.C. Van Wolput, J.P. Wolthuizen, J.H.C. Van Hooff, J. Chem. Soc. Faraday Trans. 90 (1994) 1033.
[82] A.R. West, Basic Solid State Chemistry, Wiley, Chichester, 1988.
[83] A.N. Cormack, G.V. Lewis, S.C. Parker, C.R.A. Catlow, J. Phys. Chem. Solids 49 (1988) 53.
[84] D.R. Lide, CRC Handbook of Chemistry and Physics, 75th Edition, CRC Press, Boca Raton, 1994.
[85] M. Huang, S. Kaliaguine, Stud. Surf. Sci. Catal. 78 (1993) 559.
[86] D.H. Olsen, Zeolites 15 (1995) 439.
[87] L. Campana, A. Selloni, J. Weber, A. Goursot, J. Phys. Chem. B 101 (1997) 9932.
[88] A. Goursot, V. Vasilyev, A. Arbuznikov, J. Phys. Chem. B 101 (1997) 6420.
[89] R.Ch. Deka, K. Hirao, J. Mol. Catal. A 181 (2002) 275.
[90] C. Mellot-Draznieks, S. Buttefey, A. Boutin, A.H. Fuchs, Chem. Commun. (2001) 2200.
[91] J.M. Newsam, C.M. Freeman, A.M. Gorman, B. Vessal, Chem. Commun. (1996) 1945.
[92] A.R. Ruiz-Salvador, D.W. Lewis, J. Rubayo-Soneira, G. Rodriguez-Fuentes, J. Phys. Chem. B 102 (1998) 8417.
[93] M. Stöcker, Micropor. Mesopor. Mater. 29 (1999) 3.
[94] B.V. Vora, T.L. Marker, P.T. Berger, H.R. Nilsen, S. Kvisle, T. Fuglerud, in: M. de Pontes, R.L. Espinoza, C.P. Nicolaides, J.H. Scholz, M.S. Scurrell (Eds.), Studies Surface Science Catalysis, Vol. 107, Elsevier, Amsterdam, 1997, p. 87.
[95] P.B. Weisz, Pure Appl. Chem. 52 (1980) 2091.
[96] P.B. Weisz, W.O. Haag, R.M. Lago, Nature 309 (1984) 589.
[97] S. Hoèevar, J. Batista, V. Kauèiè, J. Catal. 139 (1993) 351.
[98] C. de las Pozas, R. Lopez-Cordero, J.A. Gonzalez-Morales, N. Travieso, R. Roque-Malherbe, J. Mol. Catal. 83 (1993) 145.
[99] H. Nur, H. Hamdan, Mater. Res. Bull. 36 (2001) 315.
[100] J.A. Rabo, G.J. Gajda, Catal. Rev. Sci. Eng. 31 (1989) 385.
[101] P. Ugliengo, B. Civalleri, C.M. Zicovich-Wilson, R. Dovesi, Chem. Phys. Lett. 318 (2000) 247.
[102] A.P. Scott, L. Radom, J. Phys. Chem. 100 (1996) 16502.
[103] G. Lischke, B. Parlitz, U. Lohse, E. Schreier, R. Fricke, Appl. Catal. A: General 166 (1998) 351.
[104] G. Sastre, D.W. Lewis, J. Chem. Soc. Faraday Trans. 94 (1998) 3049.
[105] D.W. Lewis, G. Sastre, Chem. Commun. (1999) 349.
[106] H.G. Karge, V. Dondur, J. Phys. Chem. 94 (1990) 765.
[107] H.G. Karge, V. Dondur, J. Weitkamp, J. Phys. Chem. 95 (1991) 283.
[108] J. Jänchen, M.J. Haanepen, M.P.J. Peeters, J.H.M.C. van Wolput, J.P. Wolthuizen, J.H.C. van Hooff, in: J. Weitkamp, H.G. Karge, H. Pfeifer, W. Hölderich (Eds.), Zeolites and Related Microporous Materials: State of the Art 1994 Studies in Surface Science and Catalysis, Vol. 84, Elsevier Science, Amsterdam, 1994.
[109] F. Corà, I. Saadoune, C.R.A. Catlow, Angew. Chem. Int. Ed. 41 (2002) 4677.
[110] J. Chen, J.M. Thomas, G. Sankar, J. Chem. Soc. Faraday Trans. 90 (1994) 3455.
[111] P.A. Barrett, G. Sankar, R.H. Jones, C.R.A. Catlow, J.M. Thomas, J. Phys. Chem. B 101 (1997) 9555.
[112] U. Schuchardt, D. Cardoso, R. Sercheli, R. Pereira, R.S. da Cruz, M.C. Guerreiro, D. Mandelli, E.V. Spinacé, E.L. Pires, Appl. Catal. A: General 211 (2001) 1.
[113] J.M. Thomas, R. Raja, G. Sankar, R.G. Bell, Nature 398 (1999) 227.
[114] F.J. Luna, S.E. Ukawa, M. Wallau, U. Schuchardt, J. Mol. Catal. A 117 (1997) 405.
[115] F. Corà, C.R.A. Catlow, A. D'Ercole, J. Mol. Catal. A 166 (2001) 87.
[116] B. Notari, Adv. Catal. 41 (1996) 253.
[117] I.W.C.E. Arends, R.A. Sheldon, M. Wallau, U. Schuchardt, Angew. Chem. Int. Ed. Engl. 36 (1997) 1144.
[118] P.E. Sinclair, G. Sankar, C.R.A. Catlow, J.M. Thomas, T. Maschmeyer, J. Phys. Chem. B 101 (1997) 4232.
[119] G. Ricchiardi, A. de Man, J. Sauer, Phys. Chem. Chem. Phys. 2 (2000) 2195.
[120] P.E. Sinclair, C.R.A. Catlow, J. Chem. Soc. Chem. Commun. (1997) 1881.
[121] J.M. Thomas, G. Sankar, Acc. Chem. Res. 34 (2001) 571.
[122] T. Maschmeyer, F. Rey, G. Sankar, J.M. Thomas, Nature 378 (1995) 159.
[123] A. Jensen, Theor. Chim. Acta 63 (1983) 269.
[124] T.A. Halgren, W.N. Lipscomb, Chem. Phys. Lett. 49 (1977) 225.
[125] C.M. Barker, Ph.D. Thesis, University of London, 2001.
[126] A. Bhaumik, T. Tatsumi, J. Catal. 176 (1998) 305.
[127] M.G. Clerici, G. Bellussi, U. Romano, J. Catal. 129 (1991) 159.